Research paper

Using sea-floor morphometrics to constrain stratigraphic models of sinuous submarine channel systems

Aaron P. Reimchen [a, *], Stephen M. Hubbard [a], Lisa Stright [b], Brian W. Romans [c]

[a] Department of Geoscience, University of Calgary, Calgary, Alberta, T2N 1N4, Canada
[b] Department of Geosciences, Colorado State University, Fort Collins, CO, 80523-1482, USA
[c] Department of Geosciences, Virginia Polytechnic Institute and State University, Blacksburg, VA, 24061, USA

ABSTRACT

Constructing geologically accurate reservoir models of deep-water strata is challenging due to the reliance on incomplete or limited resolution datasets. Connecting areas of high-certainty across areas where data is sparse or non-existent (e.g., between wellbores) is difficult and requires numerous interpretations and assumptions. In this study, morphometric data from the Lucia Chica Channel System, offshore California, provides high-resolution 3-D information that is used to constrain correlation and characterization of ancient submarine channel fill deposits.

A statistical relationship between cross-sectional asymmetry and planform morphology in sinuous submarine channels is determined from bathymetric data. Submarine channel cross-sectional asymmetry was quantified by calculating the ratio between the distance from the inner bend margin to the thalweg by the entire channel width. This metric was calculated for 243 cross-sections, from 27 channel bends ranging in sinuosity from 1.0 to 3.0. Three distinct channel geometries are classified based on their thalweg position; normal asymmetrical, symmetrical and inverse asymmetrical. Straight channel segments (sinuosities 1.0–1.05) exhibit the most symmetrical cross-sectional morphologies. Low (sinuosities 1.05–1.2) and high sinuosity (sinuosities >1.2) channel bends exhibit maximum cross-sectional asymmetries at bend apexes, with symmetrical cross-sectional morphologies at inflection points. As expected, asymmetry values systematically increase from straight to high sinuosity channel segments; however, the most significant increase occurs at the threshold from straight to low sinuosity channel segments, which suggests that even minor deviation from straight channels promotes development of asymmetrical cross-sectional morphologies. Defined relationships are utilized to inform correlation of channelform surfaces between two well-exposed outcrops of a sinuous deep-water channel system that are ~1 km apart (Cretaceous Tres Pasos Formation, southern Chile). The developed methodology can be applied in the subsurface to model realistic channelform sedimentary bodies guided by channel planform interpretations from limited-resolution 3-D seismic data, augmented by well data.

© 2016 Elsevier Ltd. All rights reserved.

1. Introduction

Submarine channel systems are important conveyers of sediment from shallow- to deep-marine settings (Normark, 1970; Mutti and Normark, 1987; Kolla et al., 2001; Deptuck et al., 2003; Mayall et al., 2006; Gee et al., 2007; Covault et al., 2012; Sylvester et al., 2012). The deposits of ancient submarine channels contain significant volumes of hydrocarbon resources, and extensive subsurface data collection, along with enhanced visualization techniques over

the past three decades, have improved our understanding of these depositional systems (Pirmez et al., 2000; Abreu et al., 2003; Samuel et al., 2003; Mayall et al., 2006; Deptuck et al., 2007; Kolla et al., 2007; Sylvester et al., 2011). Building accurate 3-D models of submarine channel strata for use in paleoenvironment interpretation and reservoir modeling is difficult as a result of incomplete datasets. For example, outcrops offer high-resolution perspectives of stratigraphy, but exposures are inherently discontinuous as a result of larger-scale geology (e.g., fold-thrust belt segmentation) and cover (e.g., vegetation). Therefore, constraining stratigraphic architecture of channelized sedimentary bodies amongst outcrop locations commonly requires interpretations and

assumptions about length-scales and geometries of distinct lith-ofacies (e.g., Pyles et al., 2010; Pringle et al., 2010; Moody et al., 2012; Macauley and Hubbard, 2013). Subsurface datasets are more continuous, but are typically integrated across a range of disconnected scales, from centimeter-scale core analysis to inter-pretation of decameter-scale seismic reflection data (Abreu et al., 2003; Posamentier and Kolla, 2003; Deptuck et al., 2003; De Ruig and Hubbard, 2006; Cross et al., 2009). Constraining stratigraphic architecture of reservoir bodies is difficult because features such as individual slope channel fills commonly fall between the resolution of core and seismic datasets.

Morphologic data from fluvial channels, such as meander wavelength, sinuosity, and channel width-to-depth ratio, have been compiled for decades (e.g., Leopold and Wolman, 1960; Brice, 1974; Hickin, 1974; Hickin and Nanson, 1975; Hudson and Kesel, 2000). Quantitative analyses of geometries in submarine channel systems have been of more recent interest, emphasizing metrics that were developed for analyzing fluvial systems (cf. Flood and Damuth, 1987; Clark et al., 1992; Clark and Pickering, 1996; Kolla et al., 2001, 2007; Wynn et al., 2007). These studies of submarine channels, however, lack the detailed characterization of cross-sectional channel morphologies and their relationship to channel sinuosity. This important information provides constraints for reconstructing the shape of channel bodies in the stratigraphic record. The magnitude of cross-sectional asymmetry is presumed to be proportional to the magnitude of sinuosity (e.g., Peakall et al., 2000; Abreu et al., 2003; Deptuck et al., 2007). This relationship is recognized based on composite channelforms described from

stratigraphic data (Fig. 1; cf. Posamentier and Kolla, 2003; Dixon, 2003; Deptuck et al., 2003, 2007; Mayall et al., 2006; Pyles, 2008; Jobe et al., 2015); however, it has not been statistically demon-strated from morphologic information constrained by bathymetric data.

In this study we derive mathematical relationships between sinuous slope channel planform morphology and cross-sectional geometry using high-resolution bathymetric data from the Lucia Chica Channel System (LCCS), offshore central California. The re-sults are used to condition channel body geometries between disconnected outcrop exposures of slope strata in Chilean Patago-nia (Cretaceous Tres Pasos Formation). This analysis will highlight the implications of utilizing geomorphic surfaces in the interpre-tation of the stratigraphic record and help shed light on formative channel processes on the slope. The developed workflow can also be applied in order to inform the shape and spatial relationships of channel bodies in reservoir models constrained by limited well penetrations and seismic data.

2. Sinuous deep-water channels

Submarine channels extend from the shelf edge to the deep-sea along continental slopes, and are common to water depths from 1 to 4 km (cf. Deptuck et al., 2003; Gee et al., 2007; Wynn et al., 2007). Many channels are represented by negative relief expressions on the seafloor that are produced and later modified by sediment density flow events (Mutti, 1977; Mutti and Normark, 1987). The geomorphic features are typically a long-term conduit through
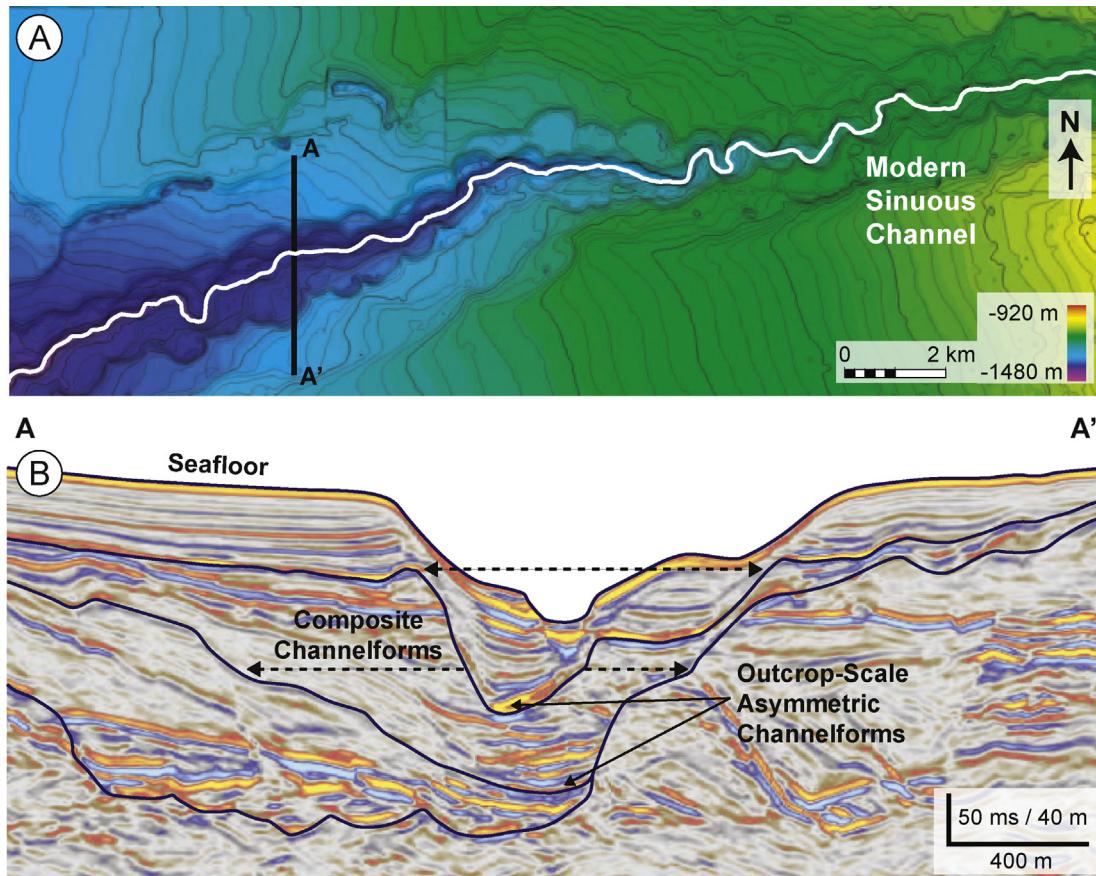
**Fig. 1.** Example of a sinuous deep-water slope channel from the Niger Delta Slope. (A) Sea-floor bathymetry map illustrating the sinuous nature of the modern slope channel (Modified from Jobe et al., 2015). (B) Seismic cross-section illustrating large composite asymmetrical channelforms that contain smaller (outcrop scale) asymmetrical channel fills. Cross-section location illustrated in Part A (Modified from Jobe et al., 2015).

which sediment is transported downslope (Wynn et al., 2007; Hubbard et al., 2014). The negative relief can be generated and maintained through mass wasting, erosional, or depositional processes as a result of auto- and/or allogenic factors (Mutti and Normark, 1987; Gee et al., 2006; Alves, 2010; Fildani et al., 2013; Covault et al., 2014; Jobe et al., 2015). Cross-sectional asymmetry in submarine channel fills has been described from numerous outcrop (Campion et al., 2000; Sullivan et al., 2000; Lien et al., 2003; Pyles et al., 2010) and seismic reflection studies (Abreu et al., 2003; Deptuck et al., 2007; Kolla et al., 2007; Babonneau et al., 2010). On the seafloor, asymmetrical channels are characterized by a thalweg position that deviates from the centerline of the channel, situated more proximal to one channel edge. In contrast, symmetrical channels exhibit similar thalweg and channel centerline positions.

In planform, submarine channels typically display sinuous morphology as they transect the slope (Fig. 1A) (e.g., Damuth and Flood, 1984; Clark and Pickering, 1996; Babonneau et al., 2002; Deptuck et al., 2003; Mayall et al., 2006; Kolla et al., 2012). Sinuosity is the ratio between the length along the channel axis to the straight line distance between the two end points; therefore, a sinuosity of 1.0 represents a straight segment and values over 1.0 reveal a deviation from straight into sinuous forms. Clark et al. (1992) and Clark and Pickering (1996) suggest sinuosities greater than approximately 1.15 define a sinuous channel, while Wynn et al. (2007) propose a minimum average sinuosity of 1.2. For the purposes of this study a three-fold classification scheme is presented, with straight channels defined by sinuosities between 1.0 and 1.05, low sinuosity channels between 1.05 and 1.2 and high sinuosity channels greater than 1.2. These defined sinuosity thresholds better characterize the measured sinuosities from submarine channel systems in this study, and are comparable with values used in previous analyses of submarine systems (cf. Clark et al., 1992; Clark and Pickering, 1996; Posamentier and Kolla, 2003; Gee et al., 2007; Wynn et al., 2007; Janocko et al., 2013a).

Modern sinuous submarine channel systems have been documented globally, including the extensively studied Amazon (Flood and Damuth, 1987; Pirmez and Flood, 1995; Pirmez and Imran, 2003), Mississippi (Kastens and Shor, 1986; Pickering et al., 1986), Zaire/Congo (Savoye et al., 2000; Babonneau et al., 2002, 2010; Ferry et al., 2005), Bengal (Hubscher et al., 1997; Schwenk et al., 2003), Indus (Kolla and Coumes, 1987), and Rhone Fans (Droz and Bellaiche, 1985; Torres et al., 1997). Ancient systems exhibit similar sinuous planform expressions, mapped in 3-D seismic reflection data (Kolla et al., 2001; Posamentier and Kolla, 2003; Deptuck et al., 2003; Gee et al., 2007; Cross et al., 2009; Nakajima et al., 2009; Catterall et al., 2010; Kolla et al., 2012), and outcrop (Beaubouef et al., 2000; Pyles et al., 2010; Moody et al., 2012; Hubbard et al., 2014).

3. Study area and dataset

This study focuses on a series of mid-slope channels informally termed the Lucia Chica Channel System (LCCS) (cf. Maier et al., 2011, 2012, 2013; Fildani et al., 2013). Multibeam bathymetry offshore central California shows the channel system bisecting the Sur Pockmark Field in the structurally controlled Sur Basin (Fig. 2) (cf. McCulloch, 1987; Paull et al., 2002; Greene et al., 2002). The LCCS is located in water depths ranging from 950 to 1250 m, and is composed of four channels formed through a series of avulsions, with the most recent channel present in the north (Maier et al., 2011). The channels converge downslope of the study area and join the Lucia Canyon at ~1850 m water depth (cf. Maier et al., 2012). For this study, approximately 70 km^2 of bathymetry data from an Autonomous Underwater Vehicle (AUV), with 1 m lateral

and 30 cm vertical resolution, was utilized to characterize channel morphologies.

4. Methods

The bathymetric data were collected by the Monterey Bay Aquarium Research Institute between 2007 and 2009 (refer to Maier et al., 2011 for details of data acquisition and processing). Channel edges and thalweg positions were mapped for three of the channels in the LCCS (Fig. 2). The fourth channel in the northern part of the study area represents the youngest phase of channelization (Maier et al., 2011) and is not considered in this analysis since it is interpreted to represent an incomplete channel that did not fully develop as a result of system shutoff during the Holocene (cf. Maier et al., 2013). Prior to collecting morphologic data, channel thalweg lines were mapped from the bathymetric surface using 3-D visualization software (Fig. 3A). Georeferenced thalweg lines were transformed to a reference origin (0, 0) and rotated until the two inflection points were at the same Y_2 value (Fig. 3B—D), allowing for consistent analysis between all analyzed channel segments. Bend apexes were subsequently delineated where the first derivative of the rotated thalweg line equaled zero (Fig. 3D).

The cumulative arc lengths of each channel bend were calculated and the distances between the apex and two inflection points upslope and downslope were determined. These distances were then used to calculate the spacing of a series of cross-sections (Fig. 2C, D). Across-channel, strike-oriented cross-sections were taken at each bend apex and at 4 evenly spaced locations upslope and downslope of the bend apex; therefore, each individual bend includes 9 total cross-sections (Fig. 3E). For each bend, cross-sections were grouped with respect to the position along the channel bend (1—4 upslope, 5 apex, and 6—9 downslope). Once the cross-section locations were determined, the bathymetric surface was analyzed. Channel metrics determined include: (1) channel width, (2) distance from the inner margin of a bend to thalweg, and (3) relief from thalweg to channel edge. The degree of cross-sectional asymmetry is described by the ratio between the distance from the inner bend margin to the thalweg versus the entire channel width (1), where A_y is the calculated asymmetry, D_t is the distance to the thalweg from the inner margin, and w is the channel width.

$$A_y = D_t/w \qquad (1)$$

This dimensionless number quantifies the degree of cross-sectional asymmetry and can indicate the position of the thalweg from the inner margin with a known channel width. The calculated asymmetry values were then tabulated (Table 1) for each individual bend and analyzed based on distance from bend apexes.

Distances of cross-sections from the bend apex are normalized for the direct comparison of channel bends with differing arc lengths. The distances were normalized by dividing the arc length of the segment from the bend apex to the analyzed cross-section location by the cumulative arc length of the entire bend. This normalized distance value is negative for upslope positions and positive for downslope positions. In addition to asymmetry values, sinuosities were calculated for each analyzed bend. In total, 34 channel bends were analyzed and 306 cross-sections measured (Table 1). Of the 34 analyzed bends, 7 were manually removed as a result of: atypical thalweg pathways generated through multiple phases of channelization (CH1-B1, CH1-B3); poorly defined thalwegs within the most upslope segments of each channel (CH2-B1, CH3-B1, CH3-B2, CH3-B3); and acquisition artifacts within the bathymetric dataset (CH3-B12). The analyzed 27 bends were subsequently transformed and rotated to determine bend apexes
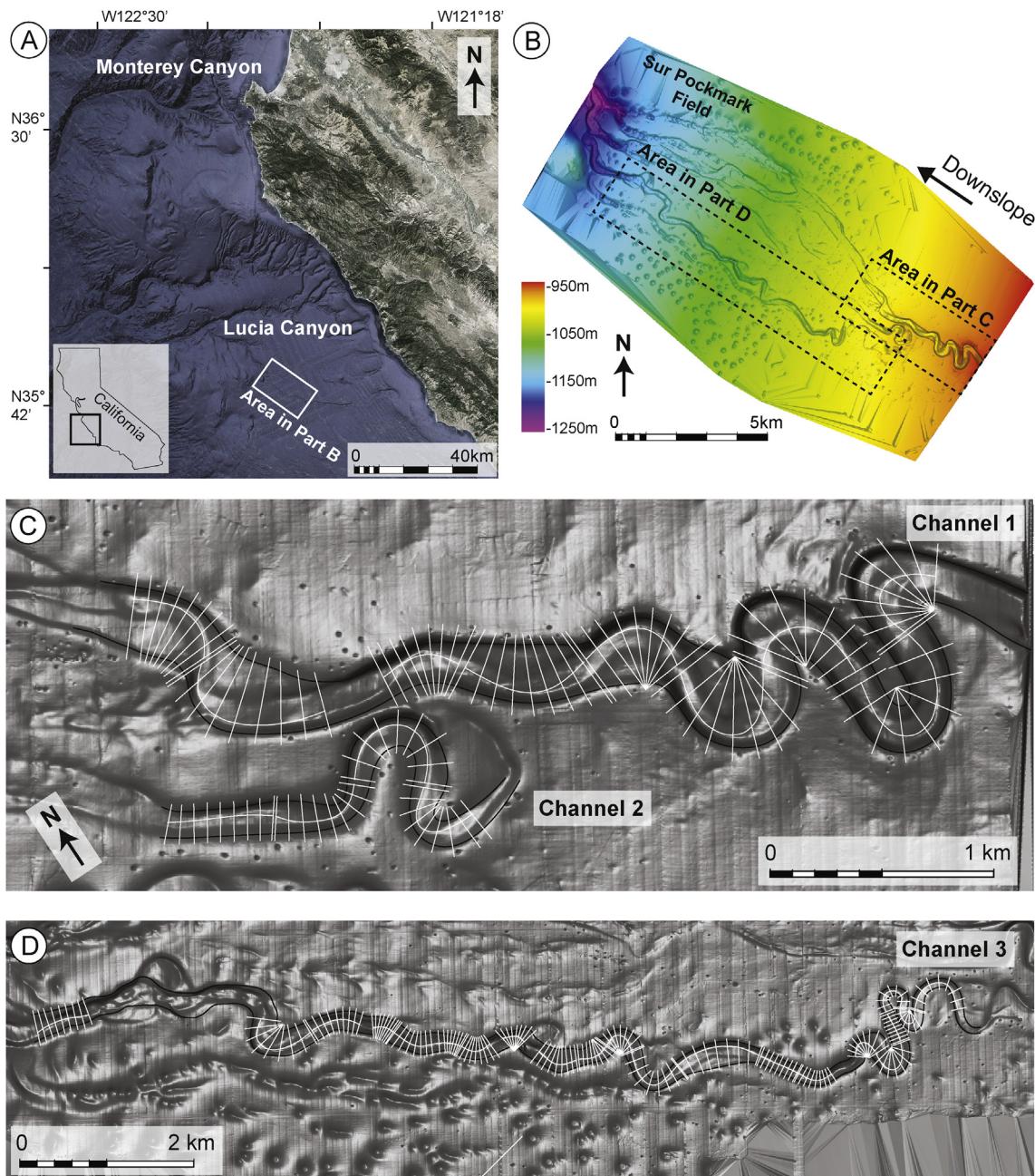
Fig. 2. (A) Study area location offshore central California (Map data: Google, CSUMB SFML, CA OPC, MBARI). White box denotes the location of the Lucia Chica Channel System illustrated in Part B. (B) Autonomous underwater vehicle (AUV) multibeam bathymetric data. Dashed black boxes denote zoomed in areas in Parts C and D. (C, D) Zoomed in sea-floor images of the 3 analyzed channels. In total 34 channel bends were analyzed with 306 cross-sections measured.

(Fig. 4A–C).

5. Results

5.1. Sinuosity

Overall, the submarine channel system comprises segments with sinuosities ranging from 1.0 to 3.0 (Table 1). Of the 27 total analyzed bends, 6 channel segments (22%) are considered straight with sinuosities from 1 to 1.05, 11 (41%) exhibit low sinuosities ranging from 1.05 to 1.2, and 10 (37%) display high sinuosities greater than 1.2 (Fig. 4D). The channels do not demonstrate downslope sinuosity trends. Low and high sinuous channel bends

(sinuosities >1.05) are most dominant whereas straight channel segments (sinuosities 1.0 to 1.05) are the least common.

5.2. Channel morphologies

LCCS submarine channels are concave upward, V- or U-shaped in cross-section, and generally characterized by a slightly rugose to smooth basal surface. The thalweg or axis of a channel can be narrow (<5 m) or broad (50 m), with channel margins occasionally characterized by terraces or steps. Channel widths in the LCCS range from 100 to 500 m (average 195 m) with up to 20 m of relief, and aspect-ratios ranging from 10 to 80 (average 23) (Table 1).

Three channel morphologies are classified based on the location
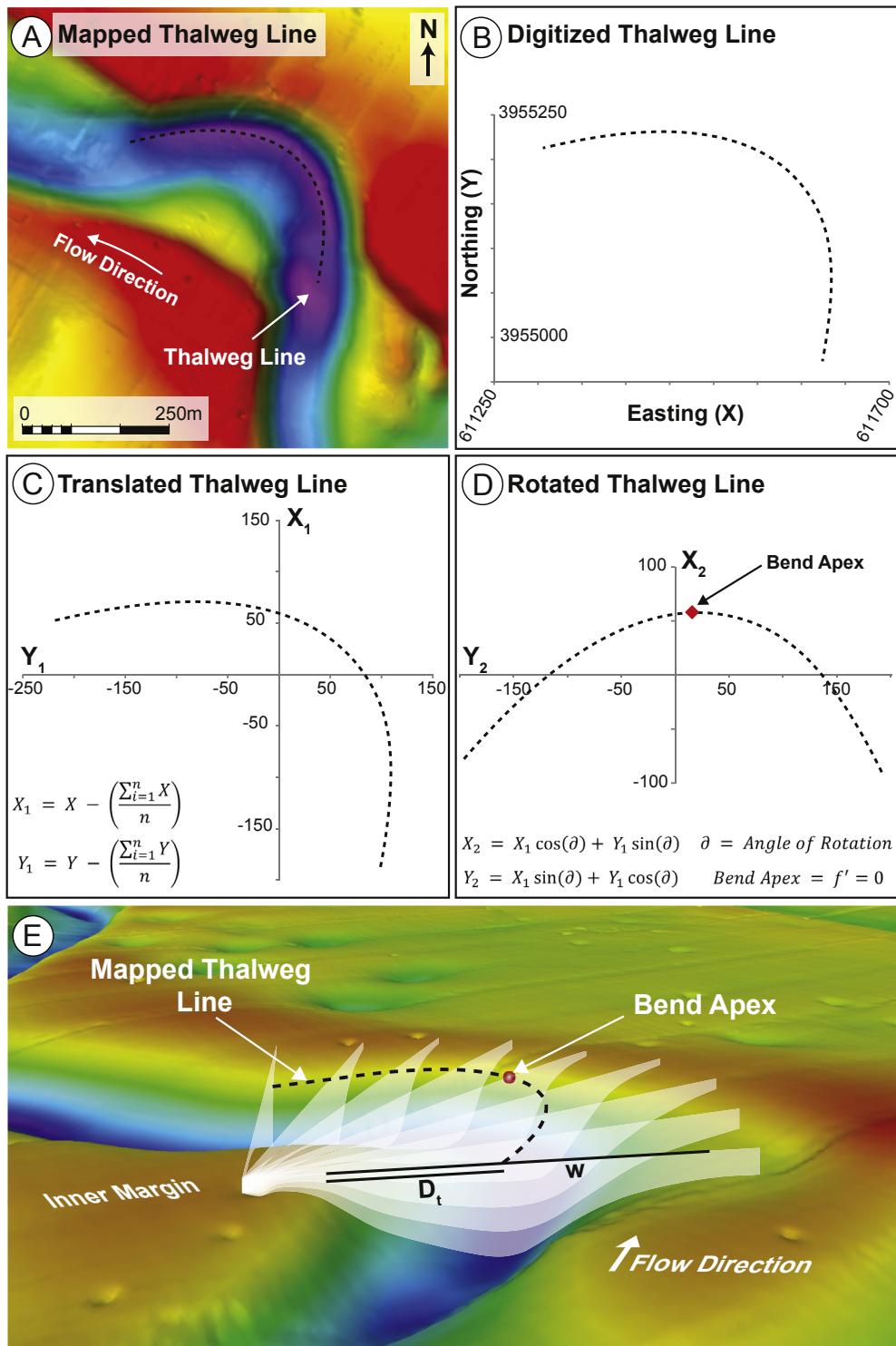
Fig. 3. Methods of analysis. (A) Planform bathymetric image of an analyzed channel bend and mapped thalweg line. (B) Georeferenced channel thalweg that was subsequently (C) transformed to a reference origin (0, 0), and (D) rotated until the two inflection points were at the same Y2 value to determine the bend apex and cross-section locations. (E) Perspective image looking downslope of the bend illustrated in Part A. Nine evenly spaced cross-sections were measured at each bend, including one at the bend apex. Each cross section was grouped based on its position with respect to the apex (1—4 upslope and 6—9 downslope). The measured channel width (w) and distance to the thalweg from the inner bend margin (D_t) are illustrated.

of the thalweg with respect to the inner bend margin. The measured geometries are herein referred to as normal asymmetric, symmetric, and inverse asymmetric (Fig. 5). Normal asymmetrical channels are the typical channel morphologies observed around

sinuous channel bends and have been described from numerous stratigraphic datasets (Campion et al., 2000; Sullivan et al., 2000; Babonneau et al., 2002; Deptuck et al., 2007). The calculated asymmetry values for these forms are greater than 0.55, indicating

Table 1
Cross-sections and calculated channel morphometrics.

Group	Bend	Cross-section	Arc length	Distance from apex	Normalized distance	Channel width	Distance to thalweg	Asymmetry	Incision	Aspect-ratio	Sinuosity
1*	CH1-B1	C1-1	494	−260	−0.5	173	122	0.71	5.8	29.9	1.8
1	CH1-B2	C1-10	889	−470	−0.5	184	89	0.48	7.3	25.3	3.0
1*	CH1-B3	C1-19	594	−310	−0.5	164	109	0.66	10.3	15.9	1.5
1	CH1-B4	C1-28	744	−359	−0.5	267	104	0.39	8.9	30.1	2.1
1	CH1-B5	C1-37	519	−255	−0.5	177	104	0.59	16.5	10.7	1.3
1	CH1-B6	C1-46	590	−275	−0.5	184	136	0.74	12.7	14.5	1.1
1	CH1-B7	C1-55	365	−175	−0.5	192	88	0.46	10.8	17.7	1.1
1	CH1-B8	C1-64	761	−406	−0.5	178	137	0.77	8.6	20.6	1.3
1	CH1-B9	C1-73	467	−230	−0.5	188	116	0.62	5.0	37.2	1.2
1*	CH2-B1	C2-1	441	−235	−0.5	112	39	0.35	3.6	31.3	1.8
1	CH2-B2	C2-10	671	−330	−0.5	155	84	0.55	4.8	32.5	2.2
1	CH2-B3	C2-19	441	−190	−0.4	131	70	0.53	7.4	17.7	1.2
1	CH2-B4	C2-28	465	−207	−0.4	168	89	0.53	9.4	17.8	1.0
1*	CH3-B1	C3-1	855	−410	−0.5	202	48	0.24	2.5	79.5	1.8
1*	CH3-B2	C3-10	425	−195	−0.5	135	87	0.64	1.5	90.6	2.5
1*	CH3-B3	C3-19	570	−290	−0.5	92	34	0.37	0.9	100.1	3.5
1	CH3-B4	C3-28	645	−330	−0.5	170	100	0.59	7.0	24.2	2.1
1	CH3-B5	C3-37	370	−185	−0.5	181	92	0.51	10.1	18.0	1.7
1	CH3-B6	C3-46	405	−190	−0.5	143	68	0.48	11.1	12.8	1.1
1	CH3-B7	C3-55	985	−500	−0.5	183	127	0.70	5.4	34.0	1.1
1	CH3-B8	C3-64	845	−400	−0.5	193	112	0.58	5.1	37.4	1.6
1	CH3-B9	C3-73	425	−225	−0.5	213	91	0.43	7.2	29.4	1.5
1	CH3-B10	C3-82	360	−170	−0.5	199	108	0.54	6.2	32.1	1.1
1	CH3-B11	C3-91	475	−230	−0.5	158	91	0.57	7.1	22.4	1.1
1*	CH3-B12	C3-100	260	−110	−0.4	202	66	0.32	11.6	17.5	1.1
1	CH3-B13	C3-109	355	−180	−0.5	172	94	0.55	14.9	11.5	1.1
1	CH3-B14	C3-118	210	−95	−0.5	177	91	0.51	14.2	12.5	1.0
1	CH3-B15	C3-127	560	−275	−0.5	188	100	0.53	12.0	15.7	1.1
1	CH3-B16	C3-136	250	−125	−0.5	206	117	0.57	15.6	13.2	1.0
1	CH3-B17	C3-145	570	−260	−0.5	191	95	0.50	15.4	12.4	1.1
1	CH3-B18	C3-154	945	−525	−0.6	204	132	0.65	6.8	29.9	1.7
1	CH3-B19	C3-163	619	−275	−0.4	212	127	0.60	18.4	11.5	1.0
1	CH3-B20	C3-172	459	−204	−0.4	175	113	0.64	8.3	21.0	1.0
1	CH3-B21	C3-181	339	−151	−0.4	103	46	0.45	3.1	33.1	1.0
2*	CH1-B1	C1-2	494	−195	−0.4	198	145	0.73	6.1	32.7	1.8
2	CH1-B2	C1-11	889	−352	−0.4	183	146	0.80	11.0	16.6	3.0
2*	CH1-B3	C1-20	594	−232	−0.4	161	102	0.64	10.1	16.0	1.5
2	CH1-B4	C1-29	744	−270	−0.4	322	281	0.87	9.3	34.7	2.1
2	CH1-B5	C1-38	519	−191	−0.4	188	124	0.66	14.7	12.8	1.3
2	CH1-B6	C1-47	590	−206	−0.3	211	168	0.80	12.1	17.4	1.1
2	CH1-B7	C1-56	365	−131	−0.4	183	104	0.57	11.4	16.1	1.1
2	CH1-B8	C1-65	761	−305	−0.4	197	152	0.77	7.4	26.6	1.3
2	CH1-B9	C1-74	467	−173	−0.4	217	162	0.75	5.7	38.3	1.2
2*	CH2-B1	C2-2	441	−176	−0.4	124	34	0.27	3.4	37.0	1.8
2	CH2-B2	C2-11	671	−248	−0.4	145	98	0.68	5.8	24.9	2.2
2	CH2-B3	C2-20	441	−143	−0.3	139	84	0.61	11.1	12.6	1.2
2	CH2-B4	C2-29	465	−155	−0.3	164	111	0.68	9.1	18.1	1.0
2*	CH3-B1	C3-2	855	−308	−0.4	281	182	0.65	3.7	76.2	1.8
2*	CH3-B2	C3-10	425	−146	−0.3	135	87	0.64	1.5	90.6	2.5
2*	CH3-B3	C3-20	570	−217	−0.4	178	92	0.52	3.0	59.9	3.5
2	CH3-B4	C3-29	645	−247	−0.4	187	106	0.57	7.2	26.2	2.1
2	CH3-B5	C3-38	370	−139	−0.4	237	113	0.47	10.3	23.0	1.7
2	CH3-B6	C3-47	405	−143	−0.4	150	80	0.53	10.6	14.2	1.1
2	CH3-B7	C3-56	985	−375	−0.4	188	140	0.75	5.3	35.1	1.1
2	CH3-B8	C3-65	845	−300	−0.4	330	248	0.75	5.8	56.6	1.6
2	CH3-B9	C3-74	425	−169	−0.4	226	119	0.52	7.8	29.1	1.5
2	CH3-B10	C3-83	360	−128	−0.4	206	125	0.61	7.4	27.9	1.1
2	CH3-B11	C3-92	475	−173	−0.4	167	119	0.71	7.6	21.9	1.1
2*	CH3-B12	C3-101	260	−82	−0.3	201	61	0.30	12.8	15.6	1.1
2	CH3-B13	C3-110	355	−135	−0.4	179	108	0.61	11.1	16.1	1.1
2	CH3-B14	C3-119	210	−71	−0.3	170	87	0.51	14.1	12.1	1.0
2	CH3-B15	C3-128	560	−206	−0.4	197	115	0.58	11.2	17.6	1.1
2	CH3-B16	C3-137	250	−94	−0.4	200	116	0.58	16.0	12.5	1.0
2	CH3-B17	C3-146	570	−195	−0.3	196	111	0.56	16.6	11.8	1.1
2	CH3-B18	C3-155	945	−394	−0.4	222	169	0.76	6.5	34.1	1.7
2	CH3-B19	C3-164	619	−206	−0.3	192	117	0.61	19.8	9.7	1.0
2	CH3-B20	C3-173	459	−153	−0.3	175	112	0.64	8.4	20.9	1.0
2	CH3-B21	C3-182	339	−113	−0.3	126	60	0.48	5.0	25.1	1.0
3*	CH1-B1	C1-3	494	−130	−0.3	234	96	0.41	8.2	28.6	1.8
3	CH1-B2	C1-12	889	−235	−0.3	187	138	0.74	16.0	11.6	3.0
3*	CH1-B3	C1-21	594	−155	−0.3	190	132	0.69	12.4	15.3	1.5
3	CH1-B4	C1-30	744	−180	−0.2	339	235	0.69	10.6	32.0	2.1
3	CH1-B5	C1-39	519	−127	−0.2	219	167	0.76	15.8	13.9	1.3

Table 1 (*continued*)

Group	Bend	Cross-section	Arc length	Distance from apex	Normalized distance	Channel width	Distance to thalweg	Asymmetry	Incision	Aspect-ratio	Sinuosity
3	CH1-B6	C1-48	590	−137	−0.2	230	184	0.80	12.7	18.1	1.1
3	CH1-B7	C1-57	365	−87	−0.2	180	114	0.63	11.5	15.6	1.1
3	CH1-B8	C1-66	761	−203	−0.3	244	211	0.86	9.0	27.0	1.3
3	CH1-B9	C1-75	467	−115	−0.2	238	199	0.84	6.2	38.5	1.2
3*	CH2-B1	C2-3	441	−118	−0.3	121	34	0.28	3.1	38.8	1.8
3	CH2-B2	C2-12	671	−165	−0.2	144	108	0.75	9.0	15.9	2.2
3	CH2-B3	C2-21	441	−95	−0.2	154	93	0.60	12.7	12.2	1.2
3	CH2-B4	C2-30	465	−103	−0.2	153	102	0.67	9.0	17.0	1.0
3*	CH3-B1	C3-3	855	−205	−0.2	274	206	0.75	3.7	73.5	1.8
3*	CH3-B2	C3-12	425	−97	−0.2	152	76	0.50	1.1	136.6	2.5
3*	CH3-B3	C3-21	570	−145	−0.3	178	127	0.72	4.5	39.3	3.5
3	CH3-B4	C3-30	645	−165	−0.3	202	128	0.64	7.3	27.5	2.1
3	CH3-B5	C3-39	370	−92	−0.2	238	131	0.55	10.4	22.8	1.7
3	CH3-B6	C3-48	405	−95	−0.2	156	88	0.56	12.1	12.9	1.1
3	CH3-B7	C3-57	985	−250	−0.3	219	170	0.78	4.9	44.5	1.1
3	CH3-B8	C3-66	845	−200	−0.2	388	322	0.83	5.5	70.2	1.6
3	CH3-B9	C3-75	425	−112	−0.3	230	125	0.54	9.7	23.7	1.5
3	CH3-B10	C3-84	360	−85	−0.2	206	130	0.63	6.8	30.1	1.1
3	CH3-B11	C3-93	475	−115	−0.2	178	121	0.68	7.0	25.3	1.1
3*	CH3-B12	C3-102	260	−55	−0.2	181	67	0.37	13.4	13.5	1.1
3	CH3-B13	C3-111	355	−90	−0.3	181	115	0.64	14.3	12.7	1.1
3	CH3-B14	C3-120	210	−48	−0.2	162	82	0.50	14.0	11.6	1.0
3	CH3-B15	C3-129	560	−138	−0.2	199	136	0.68	10.4	19.2	1.1
3	CH3-B16	C3-138	250	−63	−0.3	194	122	0.63	16.7	11.6	1.0
3	CH3-B17	C3-147	570	−130	−0.2	193	120	0.62	15.2	12.7	1.1
3	CH3-B18	C3-156	945	−263	−0.3	235	185	0.79	6.1	38.8	1.7
3	CH3-B19	C3-165	619	−137	−0.2	189	81	0.43	19.4	9.7	1.0
3	CH3-B20	C3-174	459	−102	−0.2	178	116	0.65	11.1	16.0	1.0
3	CH3-B21	C3-183	339	−75	−0.2	133	73	0.55	5.0	26.9	1.0
4*	CH1-B1	C1-4	494	−65	−0.1	254	70	0.27	9.1	27.9	1.8
4	CH1-B2	C1-13	889	−117	−0.1	195	138	0.71	17.3	11.3	3.0
4*	CH1-B3	C1-22	594	−77	−0.1	215	144	0.67	13.1	16.3	1.5
4	CH1-B4	C1-31	744	−90	−0.1	333	272	0.82	11.6	28.6	2.1
4	CH1-B5	C1-40	519	−64	−0.1	243	187	0.77	15.8	15.4	1.3
4	CH1-B6	C1-49	590	−69	−0.1	241	197	0.82	13.2	18.2	1.1
4	CH1-B7	C1-58	365	−44	−0.1	185	130	0.71	12.9	14.3	1.1
4	CH1-B8	C1-67	761	−102	−0.1	268	235	0.88	6.2	43.1	1.3
4	CH1-B9	C1-76	467	−58	−0.1	250	214	0.86	6.7	37.0	1.2
4*	CH2-B1	C2-4	441	−59	−0.1	123	71	0.58	3.6	34.6	1.8
4	CH2-B2	C2-13	671	−83	−0.1	152	114	0.75	8.7	17.4	2.2
4	CH2-B3	C2-22	441	−48	−0.1	168	103	0.61	12.6	13.3	1.2
4	CH2-B4	C2-31	465	−52	−0.1	143	98	0.69	8.3	17.1	1.0
4*	CH3-B1	C3-4	855	−103	−0.1	266	226	0.85	4.3	61.4	1.8
4*	CH3-B2	C3-13	425	−49	−0.1	168	35	0.21	1.0	160.6	2.5
4*	CH3-B3	C3-22	570	−72	−0.1	207	152	0.73	4.7	44.2	3.5
4	CH3-B4	C3-31	645	−82	−0.1	224	147	0.66	7.7	28.9	2.1
4	CH3-B5	C3-40	370	−46	−0.1	223	150	0.67	11.4	19.5	1.7
4	CH3-B6	C3-49	405	−48	−0.1	156	99	0.64	12.2	12.7	1.1
4	CH3-B7	C3-58	985	−125	−0.1	253	181	0.72	5.5	45.7	1.1
4	CH3-B8	C3-67	845	−100	−0.1	461	396	0.86	7.3	63.4	1.6
4	CH3-B9	C3-76	425	−56	−0.1	253	146	0.58	11.1	22.8	1.5
4	CH3-B10	C3-85	360	−43	−0.1	216	148	0.69	7.7	28.1	1.1
4	CH3-B11	C3-94	475	−58	−0.1	202	150	0.74	8.0	25.2	1.1
4*	CH3-B12	C3-103	260	−27	−0.1	156	77	0.49	15.3	10.2	1.1
4	CH3-B13	C3-112	355	−45	−0.1	185	112	0.61	15.9	11.6	1.1
4	CH3-B14	C3-121	210	−24	−0.1	153	78	0.51	13.7	11.1	1.0
4	CH3-B15	C3-130	560	−69	−0.1	206	144	0.70	9.6	21.3	1.1
4	CH3-B16	C3-139	250	−31	−0.1	186	120	0.65	17.7	10.5	1.0
4	CH3-B17	C3-148	570	−65	−0.1	177	111	0.63	12.4	14.3	1.1
4	CH3-B18	C3-157	945	−131	−0.1	250	206	0.82	5.5	45.8	1.7
4	CH3-B19	C3-166	619	−69	−0.1	181	76	0.42	17.4	10.4	1.0
4	CH3-B20	C3-175	459	−51	−0.1	169	108	0.64	10.1	16.8	1.0
4	CH3-B21	C3-184	339	−38	−0.1	137	82	0.60	6.6	20.8	1.0
4*	CH1-B1	C1-5	494	0	0.0	257	135	0.53	7.9	32.4	1.8
5	CH1-B2	C1-14	889	0	0.0	208	163	0.78	16.8	12.4	3.0
5*	CH1-B3	C1-23	594	0	0.0	229	153	0.67	12.9	17.7	1.5
5	CH1-B4	C1-32	744	0	0.0	328	276	0.84	14.5	22.7	2.1
5	CH1-B5	C1-41	519	0	0.0	240	189	0.79	15.3	15.7	1.3
5	CH1-B6	C1-50	590	0	0.0	246	200	0.81	14.7	16.8	1.1
5	CH1-B7	C1-59	365	0	0.0	175	134	0.77	13.8	12.6	1.1
5	CH1-B8	C1-68	761	0	0.0	266	218	0.82	3.8	69.3	1.3
5	CH1-B9	C1-77	467	0	0.0	262	223	0.85	6.8	38.4	1.2
5*	CH2-B1	C2-5	441	0	0.0	130	96	0.74	3.4	38.4	1.8
5	CH2-B2	C2-14	671	0	0.0	120	86	0.71	6.6	18.3	2.2
5	CH2-B3	C2-23	441	0	0.0	168	110	0.65	13.6	12.3	1.2

Table 1 (*continued*)

Group	Bend	Cross-section	Arc length	Distance from apex	Normalized distance	Channel width	Distance to thalweg	Asymmetry	Incision	Aspect-ratio	Sinuosity
5	CH2-B4	C2-32	465	0	0.0	143	99	0.69	7.3	19.7	1.0
5*	CH3-B1	C3-5	855	0	0.0	243	212	0.87	3.0	80.1	1.8
5*	CH3-B2	C3-15	425	0	0.0	33	14	0.42	0.4	80.9	2.5
5*	CH3-B3	C3-23	570	0	0.0	208	168	0.81	3.0	68.1	3.5
5	CH3-B4	C3-32	645	0	0.0	228	170	0.75	6.5	35.1	2.1
5	CH3-B5	C3-41	370	0	0.0	197	146	0.74	11.1	17.8	1.7
5	CH3-B6	C3-50	405	0	0.0	170	112	0.66	11.9	14.3	1.1
5	CH3-B7	C3-59	985	0	0.0	246	194	0.79	6.2	39.7	1.1
5	CH3-B8	C3-68	845	0	0.0	513	427	0.83	6.0	85.8	1.6
5	CH3-B9	C3-77	425	0	0.0	214	164	0.77	10.2	21.1	1.5
5	CH3-B10	C3-86	360	0	0.0	214	161	0.75	8.5	25.3	1.1
5	CH3-B11	C3-95	475	0	0.0	210	152	0.72	12.9	16.2	1.1
5*	CH3-B12	C3-104	260	0	0.0	143	79	0.55	16.0	8.9	1.1
5	CH3-B13	C3-113	355	0	0.0	175	104	0.59	16.0	10.9	1.1
5	CH3-B14	C3-122	210	0	0.0	148	71	0.48	13.3	11.1	1.0
5	CH3-B15	C3-131	560	0	0.0	207	146	0.71	13.6	15.2	1.1
5	CH3-B16	C3-140	250	0	0.0	183	114	0.62	18.3	10.0	1.0
5	CH3-B17	C3-149	570	0	0.0	157	104	0.66	12.1	13.0	1.1
5	CH3-B18	C3-158	945	0	0.0	236	195	0.83	6.5	36.6	1.7
5	CH3-B19	C3-167	619	0	0.0	211	101	0.48	16.1	13.1	1.0
5	CH3-B20	C3-176	459	0	0.0	165	101	0.61	9.8	16.8	1.0
5	CH3-B21	C3-185	339	0	0.0	140	85	0.61	8.1	17.2	1.0
6*	CH1-B1	C1-6	494	59	0.1	252	164	0.65	7.2	35.0	1.8
6	CH1-B2	C1-15	889	105	0.1	201	146	0.73	13.6	14.7	3.0
6*	CH1-B3	C1-24	594	71	0.1	260	125	0.48	12.9	20.2	1.5
6	CH1-B4	C1-33	744	96	0.1	214	169	0.79	13.4	16.0	2.1
6	CH1-B5	C1-42	519	66	0.1	230	178	0.77	15.9	14.5	1.3
6	CH1-B6	C1-51	590	79	0.1	237	195	0.82	14.1	16.7	1.1
6	CH1-B7	C1-60	365	47	0.1	161	121	0.76	14.4	11.2	1.1
6	CH1-B8	C1-69	761	89	0.1	200	159	0.80	3.4	59.6	1.3
6	CH1-B9	C1-78	467	59	0.1	268	227	0.85	6.6	40.8	1.2
6*	CH2-B1	C2-6	441	51	0.1	138	96	0.70	3.0	45.8	1.8
6	CH2-B2	C2-15	671	85	0.1	103	75	0.72	5.3	19.4	2.2
6	CH2-B3	C2-24	441	63	0.1	158	107	0.68	12.5	12.6	1.2
6	CH2-B4	C2-33	465	52	0.1	141	96	0.68	7.0	20.2	1.0
6*	CH3-B1	C3-6	855	111	0.1	197	168	0.85	2.4	83.4	1.8
6*	CH3-B2	C3-16	425	57	0.1	29	17	0.58	0.2	134.6	2.5
6*	CH3-B3	C3-24	570	70	0.1	102	59	0.58	1.3	81.0	3.5
6	CH3-B4	C3-33	645	79	0.1	207	169	0.81	4.9	42.2	2.1
6	CH3-B5	C3-42	370	46	0.1	186	129	0.69	9.8	19.1	1.7
6	CH3-B6	C3-51	405	54	0.1	173	110	0.64	10.3	16.8	1.1
6	CH3-B7	C3-60	985	121	0.1	190	146	0.77	5.6	33.7	1.1
6	CH3-B8	C3-69	845	111	0.1	451	411	0.91	3.8	118.1	1.6
6	CH3-B9	C3-78	425	50	0.1	212	169	0.79	8.9	23.8	1.5
6	CH3-B10	C3-87	360	48	0.1	198	158	0.80	9.8	20.2	1.1
6	CH3-B11	C3-96	475	61	0.1	183	122	0.66	12.6	14.5	1.1
6*	CH3-B12	C3-105	260	38	0.1	132	74	0.56	16.1	8.2	1.1
6	CH3-B13	C3-114	355	44	0.1	170	95	0.56	16.7	10.2	1.1
6	CH3-B14	C3-123	210	29	0.1	157	73	0.47	12.9	12.2	1.0
6	CH3-B15	C3-132	560	71	0.1	192	118	0.62	13.0	14.8	1.1
6	CH3-B16	C3-141	250	31	0.1	170	102	0.60	17.4	9.7	1.0
6	CH3-B17	C3-150	570	78	0.1	152	97	0.64	11.0	13.8	1.1
6	CH3-B18	C3-159	945	105	0.1	230	150	0.65	6.6	34.9	1.7
6	CH3-B19	C3-168	619	69	0.1	223	117	0.52	13.8	16.2	1.0
6	CH3-B20	C3-177	459	51	0.1	173	109	0.63	9.3	18.7	1.0
6	CH3-B21	C3-186	339	38	0.1	146	91	0.62	7.5	19.4	1.0
7*	CH1-B1	C1-7	494	117	0.2	203	146	0.72	7.7	26.3	1.8
7	CH1-B2	C1-16	889	210	0.2	207	105	0.51	12.1	17.1	3.0
7*	CH1-B3	C1-25	594	142	0.2	261	95	0.36	11.8	22.2	1.5
7	CH1-B4	C1-34	744	192	0.3	181	139	0.77	12.3	14.7	2.1
7	CH1-B5	C1-43	519	132	0.3	216	166	0.77	15.4	14.0	1.3
7	CH1-B6	C1-52	590	157	0.3	225	177	0.78	12.6	17.9	1.1
7	CH1-B7	C1-61	365	95	0.3	146	105	0.72	14.3	10.2	1.1
7	CH1-B8	C1-70	761	178	0.2	255	214	0.84	4.8	53.1	1.3
7	CH1-B9	C1-79	467	118	0.3	268	227	0.85	6.7	40.3	1.2
7*	CH2-B1	C2-7	441	103	0.2	133	90	0.68	3.2	41.1	1.8
7	CH2-B2	C2-16	671	170	0.3	105	72	0.68	5.3	19.7	2.2
7	CH2-B3	C2-25	441	125	0.3	158	103	0.65	10.6	14.9	1.2
7	CH2-B4	C2-34	465	103	0.2	136	87	0.64	6.4	21.3	1.0
7*	CH3-B1	C3-7	855	223	0.3	80	56	0.69	1.7	46.2	1.8
7*	CH3-B2	C3-16	425	115	0.3	29	17	0.58	0.2	134.6	2.5
7*	CH3-B3	C3-25	570	140	0.2	55	24	0.44	0.5	105.0	3.5
7	CH3-B4	C3-34	645	157	0.2	175	124	0.71	4.6	38.2	2.1
7	CH3-B5	C3-43	370	92	0.2	167	109	0.65	9.4	17.9	1.7

Table 1 (continued)

Group	Bend	Cross-section	Arc length	Distance from apex	Normalized distance	Channel width	Distance to thalweg	Asymmetry	Incision	Aspect-ratio	Sinuosity
7	CH3-B6	C3-52	405	108	0.3	173	113	0.65	8.8	19.7	1.1
7	CH3-B7	C3-61	985	243	0.2	179	140	0.78	4.3	41.7	1.1
7	CH3-B8	C3-70	845	223	0.3	136	96	0.71	5.4	24.9	1.6
7	CH3-B9	C3-79	425	100	0.2	201	153	0.76	6.8	29.4	1.5
7	CH3-B10	C3-88	360	95	0.3	172	128	0.75	9.3	18.5	1.1
7	CH3-B11	C3-97	475	123	0.3	183	114	0.62	12.3	14.9	1.1
7*	CH3-B12	C3-106	260	75	0.3	131	67	0.51	16.3	8.1	1.1
7	CH3-B13	C3-115	355	88	0.2	176	97	0.55	16.6	10.6	1.1
7	CH3-B14	C3-124	210	58	0.3	165	73	0.44	13.2	12.5	1.0
7	CH3-B15	C3-133	560	143	0.3	174	88	0.51	15.4	11.3	1.1
7	CH3-B16	C3-142	250	63	0.3	162	85	0.53	16.7	9.7	1.0
7	CH3-B17	C3-151	570	155	0.3	167	80	0.48	10.4	16.2	1.1
7	CH3-B18	C3-160	945	210	0.2	260	209	0.80	7.7	33.6	1.7
7	CH3-B19	C3-169	619	137	0.2	224	127	0.57	13.0	17.2	1.0
7	CH3-B20	C3-178	459	102	0.2	186	105	0.56	8.4	22.2	1.0
7	CH3-B21	C3-187	339	75	0.2	156	98	0.62	7.9	19.9	1.0
8*	CH1-B1	C1-8	494	176	0.4	194	138	0.72	7.5	25.9	1.8
8	CH1-B2	C1-17	889	314	0.4	153	98	0.64	12.8	12.0	3.0
8*	CH1-B3	C1-26	594	213	0.4	244	177	0.73	12.2	20.0	1.5
8	CH1-B4	C1-35	744	288	0.4	183	140	0.76	12.9	14.2	2.1
8	CH1-B5	C1-44	519	199	0.4	195	147	0.76	14.8	13.1	1.3
8	CH1-B6	C1-53	590	236	0.4	219	164	0.75	11.7	18.7	1.1
8	CH1-B7	C1-62	365	142	0.4	141	98	0.69	13.7	10.3	1.1
8	CH1-B8	C1-71	761	266	0.3	216	173	0.80	6.0	36.1	1.3
8	CH1-B9	C1-80	467	177	0.4	260	222	0.85	6.3	41.6	1.2
8*	CH2-B1	C2-8	441	154	0.3	143	88	0.62	3.6	39.1	1.8
8	CH2-B2	C2-17	671	255	0.4	116	73	0.63	5.3	22.0	2.2
8	CH2-B3	C2-26	441	188	0.4	163	108	0.66	9.8	16.6	1.2
8	CH2-B4	C2-35	465	155	0.3	145	87	0.60	5.8	25.0	1.0
8*	CH3-B1	C3-8	855	334	0.4	78	60	0.77	0.4	192.4	1.8
8*	CH3-B2	C3-17	425	172	0.4	44	27	0.61	0.4	120.4	2.5
8*	CH3-B3	C3-26	570	210	0.4	74	49	0.66	1.7	45.0	3.5
8	CH3-B4	C3-35	645	236	0.4	135	84	0.62	9.1	14.8	2.1
8	CH3-B5	C3-44	370	139	0.4	146	82	0.56	9.4	15.6	1.7
8	CH3-B6	C3-53	405	161	0.4	176	81	0.46	9.1	19.5	1.1
8	CH3-B7	C3-62	985	364	0.4	215	144	0.67	3.7	58.7	1.1
8	CH3-B8	C3-71	845	334	0.4	162	103	0.63	7.3	22.3	1.6
8	CH3-B9	C3-80	425	150	0.4	179	128	0.72	6.1	29.2	1.5
8	CH3-B10	C3-89	360	143	0.4	156	106	0.68	7.7	20.2	1.1
8	CH3-B11	C3-98	475	184	0.4	177	89	0.50	12.0	14.8	1.1
8*	CH3-B12	C3-107	260	113	0.4	131	64	0.49	15.5	8.5	1.1
8	CH3-B13	C3-116	355	131	0.4	181	93	0.51	15.7	11.5	1.1
8	CH3-B14	C3-125	210	86	0.4	175	77	0.44	13.0	13.5	1.0
8	CH3-B15	C3-134	560	214	0.4	202	99	0.49	16.6	12.2	1.1
8	CH3-B16	C3-143	250	94	0.4	159	78	0.49	16.4	9.7	1.0
8	CH3-B17	C3-152	570	233	0.4	193	82	0.43	8.9	21.7	1.1
8	CH3-B18	C3-161	945	315	0.3	252	187	0.74	8.0	31.6	1.7
8	CH3-B19	C3-170	619	206	0.3	233	152	0.65	12.7	18.3	1.0
8	CH3-B20	C3-179	459	153	0.3	185	119	0.64	9.3	19.9	1.0
8	CH3-B21	C3-188	339	113	0.3	162	102	0.63	7.3	22.3	1.0
9*	CH1-B1	C1-9	494	234	0.5	194	138	0.71	7.5	25.8	1.8
9	CH1-B2	C1-18	889	419	0.5	157	80	0.51	11.0	14.3	3.0
9*	CH1-B3	C1-27	594	284	0.5	261	206	0.79	9.5	27.4	1.5
9	CH1-B4	C1-36	744	385	0.5	170	83	0.49	15.9	10.7	2.1
9	CH1-B5	C1-45	519	265	0.5	183	137	0.75	12.7	14.4	1.3
9	CH1-B6	C1-54	590	315	0.5	197	148	0.75	11.1	17.8	1.1
9	CH1-B7	C1-63	365	190	0.5	151	84	0.56	12.3	12.3	1.1
9	CH1-B8	C1-72	761	355	0.5	196	124	0.63	4.7	41.5	1.3
9	CH1-B9	C1-81	467	236	0.5	247	166	0.67	6.7	37.1	1.2
9*	CH2-B1	C2-9	441	205	0.5	154	77	0.50	4.4	35.0	1.8
9	CH2-B2	C2-18	671	340	0.5	124	66	0.53	6.5	19.0	2.2
9	CH2-B3	C2-27	441	250	0.6	173	98	0.56	9.5	18.3	1.2
9	CH2-B4	C2-36	465	207	0.4	169	82	0.49	4.6	36.9	1.0
9*	CH3-B1	C3-9	855	445	0.5	134	87	0.65	1.4	97.0	1.8
9*	CH3-B2	C3-18	425	230	0.5	87	55	0.63	0.9	101.6	2.5
9*	CH3-B3	C3-27	570	280	0.5	86	47	0.54	2.0	43.4	3.5
9	CH3-B4	C3-36	645	315	0.5	145	59	0.41	9.5	15.3	2.1
9	CH3-B5	C3-45	370	185	0.5	143	68	0.48	11.1	12.9	1.7
9	CH3-B6	C3-54	405	215	0.5	176	64	0.36	8.1	21.8	1.1
9	CH3-B7	C3-63	985	485	0.5	192	84	0.44	3.1	61.1	1.1
9	CH3-B8	C3-72	845	445	0.5	207	117	0.57	6.9	30.0	1.6
9	CH3-B9	C3-81	425	200	0.5	195	105	0.54	6.0	32.3	1.5
9	CH3-B10	C3-90	360	190	0.5	157	103	0.65	6.9	22.8	1.1
9	CH3-B11	C3-99	475	245	0.5	175	88	0.50	12.4	14.1	1.1
9*	CH3-B12	C3-108	260	150	0.6	131	66	0.50	14.9	8.8	1.1

Table 1 (*continued*)

Group	Bend	Cross-section	Arc length	Distance from apex	Normalized distance	Channel width	Distance to thalweg	Asymmetry	Incision	Aspect-ratio	Sinuosity
9	CH3-B13	C3-117	355	175	0.5	180	87	0.49	14.5	12.4	1.1
9	CH3-B14	C3-126	210	115	0.5	179	74	0.41	10.3	17.4	1.0
9	CH3-B15	C3-135	560	285	0.5	212	95	0.45	15.2	14.0	1.1
9	CH3-B16	C3-144	250	125	0.5	179	64	0.36	16.4	10.9	1.0
9	CH3-B17	C3-153	570	310	0.5	199	100	0.50	7.5	26.4	1.1
9	CH3-B18	C3-162	945	420	0.4	220	126	0.57	9.3	23.7	1.7
9	CH3-B19	C3-171	619	275	0.4	261	168	0.64	9.8	26.6	1.0
9	CH3-B20	C3-180	459	204	0.4	188	126	0.67	8.9	21.0	1.0
9	CH3-B21	C3-189	339	151	0.4	168	102	0.60	7.2	23.5	1.0

*Removed cross-sections.
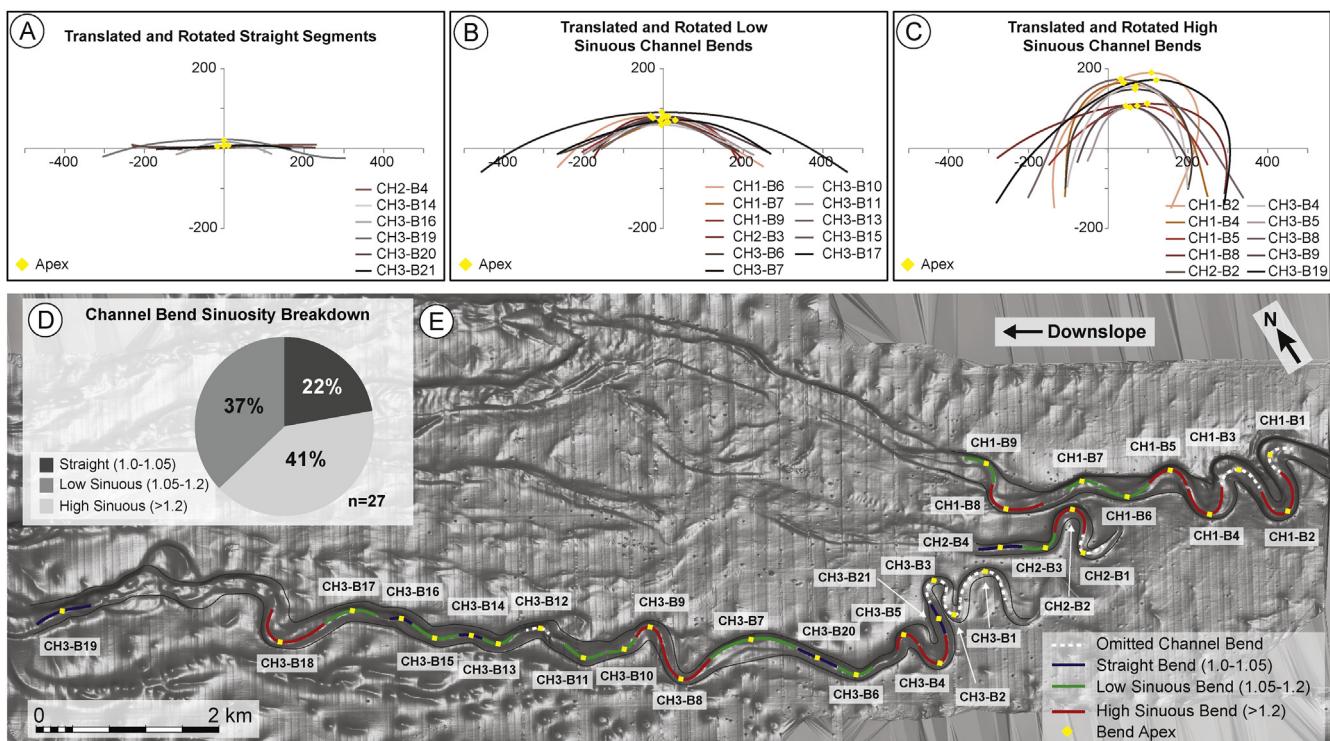
Fig. 4. Translated and rotated channel segments of (A) straight, (B) low, and (C) high sinuous bends for this analysis. (D) Cumulative pie graph illustrating the breakdown of bend sinuosities. The LCCS is a sinuous channel system with the majority of channel bends greater than 1.05. (E) Bathymetric image of the 3 analyzed channels and the individual bends within this study. See Table 1 for all the measured morphometric and sinuosity data.

the thalweg is skewed toward the outer bend margin (Fig. 5A). Symmetrical channels exhibit asymmetry values of 0.5, indicating the thalweg is aligned with the centerline of the channel (Fig. 5B). We classify any channel with asymmetry values between 0.45 and 0.55 as symmetric. Inverse asymmetrical channels exhibit thalweg positions skewed toward the inner bend margin, and are characterized by asymmetry values less than 0.45 (Fig. 5C). Of the 243 analyzed cross-sections, 185 sections (76%) are normal asymmetrical (ranging from 0.55 to 0.91, average 0.70), 45 (19%) are symmetrical and 13 (5%) are weakly inverse asymmetrical (ranging from 0.36 to 0.45, average 0.42).

5.3. Cross-sectional asymmetry distributions

Overall, straight channel segments display a unimodal and slightly negatively skewed distribution of cross-sectional asymmetry values (Fig. 6A). The population exhibits a mean asymmetry value of 0.57, with 74% of the cross-sectional asymmetries between 0.45 and 0.65. Low sinuosity channel bends exhibit a unimodal

normal distribution, with a mean asymmetry value of 0.65 and 75% of data contained between 0.55 and 0.85 (Fig. 6B). High sinuosity channel bends display a unimodal distribution that is more negatively skewed as compared to the straight channel segment population (Fig. 6C). The population exhibits a mean asymmetry value of 0.69, with 77% of the data contained within the interval ranging from 0.55 to 0.85. Overall, mean/median asymmetry values progressively increase with each increasing sinuosity population, with more asymmetrical channel cross-sections associated with higher sinuosity channel bend populations.

5.4. Channel bend morphometric characterization

Straight channel segments (sinuosities 1.0−1.05) constitute 54 of the 243 analyzed cross-sections (22%). Collectively, channel cross-section asymmetry ranges from 0.36 to 0.69 (Fig. 7A). Cross-sectional asymmetry exhibits a maximum mean value (0.59) slightly downslope of the middle of the segment (population 6). This maximum mean asymmetry value is significantly lower than
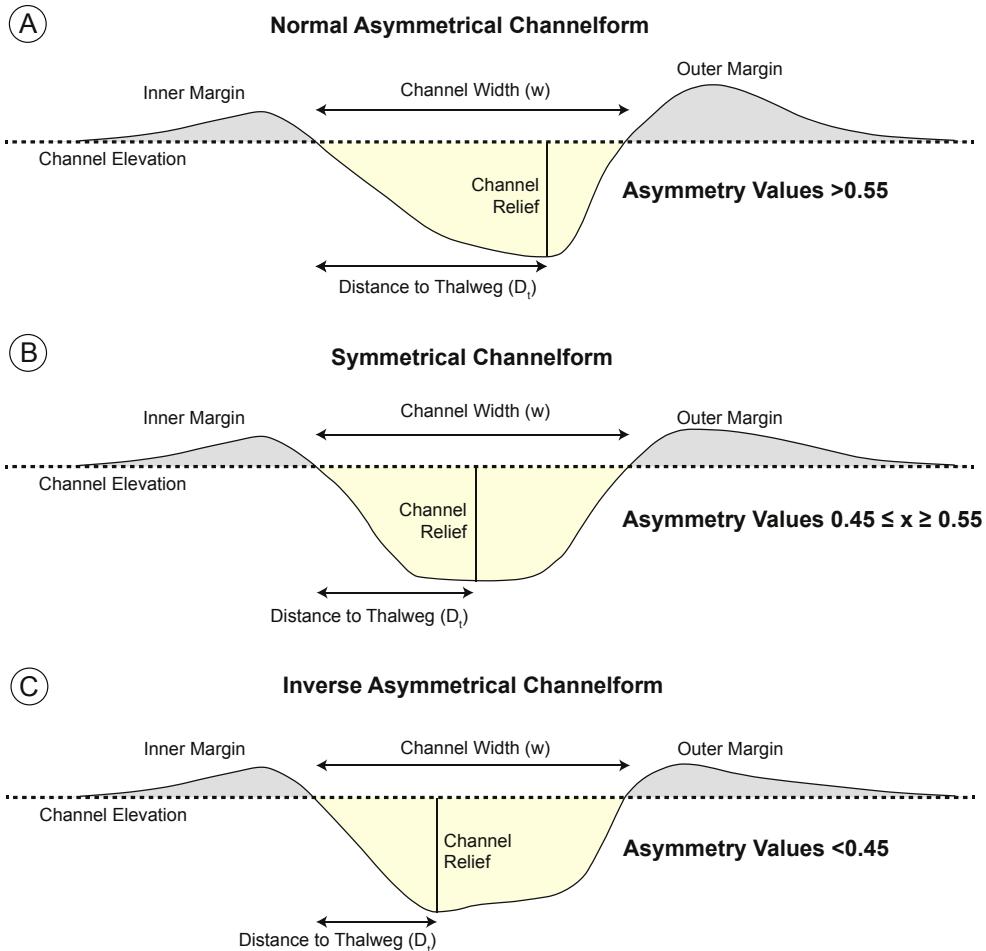
Fig. 5. The three observed channel cross-sectional morphologies measured in the Lucia Chica Channel System. (A) Normal asymmetrical channels. These forms exhibit asymmetry values greater than 0.55, indicating the thalweg is more proximal to the outer margin. (B) Symmetrical channels. Asymmetry values fall between 0.45 and 0.55, indicating the thalweg is proximal to the centerline of the channel. (C) Inverse asymmetrical channels. These forms exhibit thalweg positions more proximal to the inner margin and asymmetry values less than 0.45. The degree of cross-sectional asymmetry is described by the ratio between the distance from the inner bend margin to the thalweg (D_t) versus the entire channel width (w).

the values measured at more sinuous channel bends. In addition, straight channel segments exhibit the smallest relative change in mean asymmetry values from the two inflection points to the bend apex. From the most upslope position to the apex, the change in mean asymmetry values is 0.03. Conversely, the change in mean asymmetry values from the apex to the most downslope position is 0.05.

Low sinuosity channel bends (sinuosities 1.05–1.2) make up 99 of the 243 analyzed cross-sections (41%). Channel cross-sections are the closest to symmetrical at the inflection points, with mean asymmetry values of 0.57 and 0.54 (populations 1 and 9; Fig. 7B). Altogether, cross-sectional asymmetry is at a maximum (mean 0.72) at the bend apex (population 5); with a change in mean asymmetry from the upslope inflection position to the apex of 0.15, and from the apex to the downslope position of 0.18.

High sinuosity channel bends (sinuosities >1.2) constitute 90 of the 243 analyzed cross-sections (37%). Channel cross-sections are symmetrical at the two inflection positions, with mean asymmetry values measuring 0.55 (populations 1 and 9; Fig. 7B). Cross-sectional asymmetry values are at a maximum (mean 0.79) at the bend apex position (population 5). Overall, this population exhibits the greatest magnitude of change in asymmetry values from interbend inflection points to the apex; from the upslope position

to the apex the change is 0.23, and from the apex to the downslope position it is 0.24.

Altogether, straight channel segments exhibit the most symmetrical cross-sectional morphologies, with higher asymmetry values occurring in more sinuous channel bend populations. Low and high sinuosity channel bends exhibit comparable overall trends, with the most symmetrical channel cross-sections present at inflection points and maximum asymmetry values at bend apexes. Although rigorous comparison has not been made, cross-sectional asymmetry value distributions around a bend appear similar to what is observed in fluvial channels, with symmetrical channel morphologies only occurring at the inflection points (Leopold and Wolman, 1960; Knighton, 1981, 1982; Milne, 1983).

5.5. Quantitative channel asymmetry relationship

Calculated channel asymmetries are directly related to normalized distances away from bend apexes in a series of scatter plots (Fig. 7D–F). Negative normalized distances represent cross-sections upslope of the bend apex, where positive values indicate downslope positions. In all the analyzed channel bend populations, maximum asymmetry values are associated with the bend apex (normalized distance = 0), with values decreasing to approximately
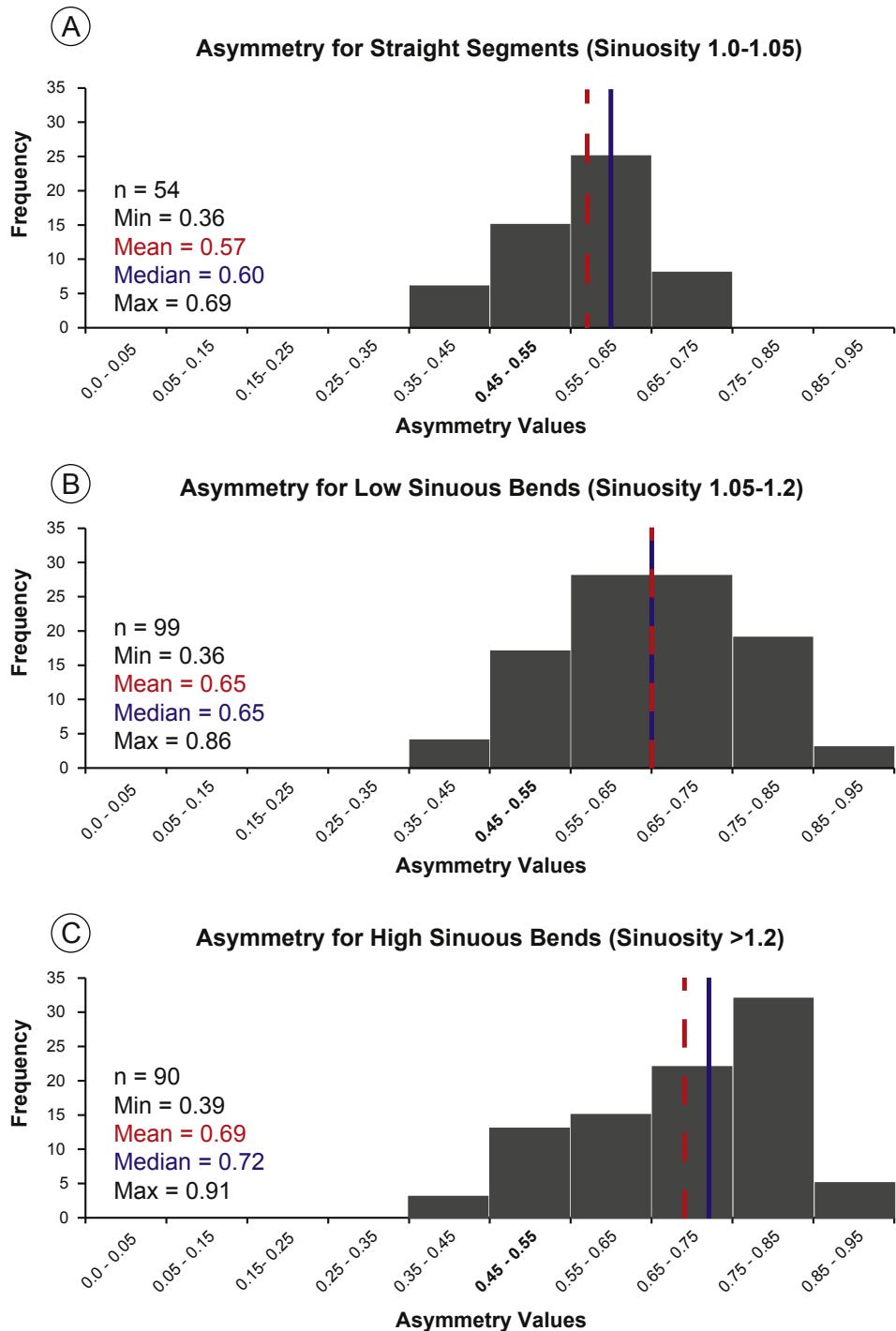
Fig. 6. Cross-sectional asymmetry value distributions based on sinuosity populations. (A) Straight (sinuosities 1.0–1.05), (B) low sinuous channel bends (sinuosities 1.05–1.2), and (C) high sinuous channel bends (sinuosities >1.2). The distributions illustrate cross-sectional asymmetries increase with increasing sinuosities. Bold values in the x-axis (0.45–0.55) represent symmetrical cross-sections.

0.5 at the distal end positions away from the apex.

Second-degree polynomial best-fit lines capture the overall convex upward trends for the data along straight channel segments (Fig. 7D), low sinuosity channel bends (Fig. 7E), and high sinuosity channel bends (Fig. 7F). These curves mathematically relate the degree of channel asymmetry to the normalized distance away from the bend apex, amongst populations defined by channel sinuosity. In these data, straight channel populations exhibit a very

slight convex upward trend with the highest data density associated with symmetrical channels (sinuosities 0.45–0.55). In addition, the polynomial curves capture the trend for both the low and high sinuous channel populations, where the most asymmetrical channel cross-sections correspond to the bend apex and symmetrical channel cross-sections at the inflection points between successive channel bends. The heat maps in Fig. 7D–F illustrate the variability of the cross-sectional asymmetry data for each sinuosity
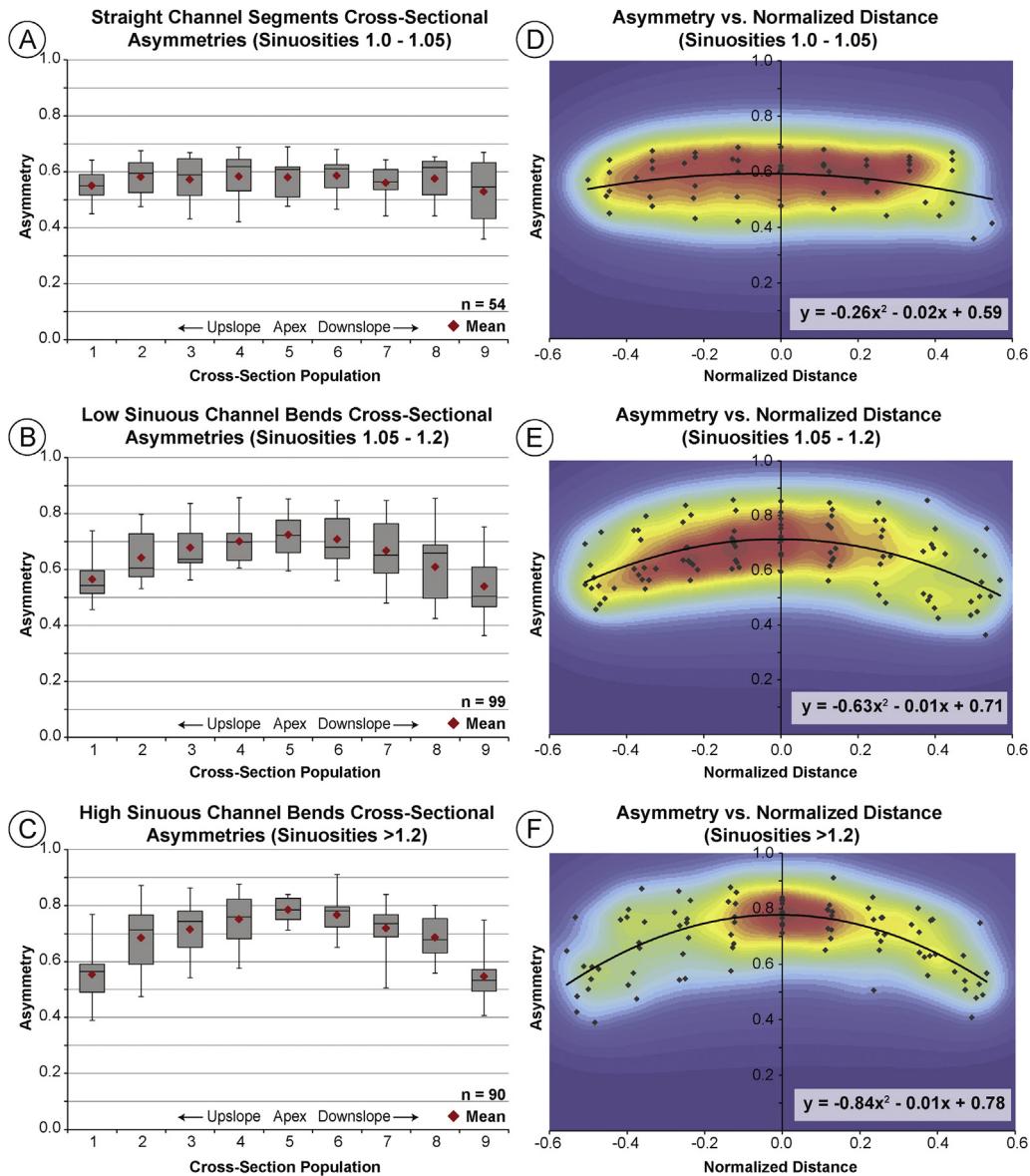
Fig. 7. (A—C) Box-and-whisker plots based on the measured bend sinuosities, illustrating the minimum, lower quartile, median, upper quartile and maximum asymmetry values measured at each cross-sectional group. Mean values for each group are demarcated by red diamonds. (D—F) Scatter plots, based on the measured bend sinuosities, relating measured asymmetry values to the normalized distances away from the bed apex. Heatmaps illustrate the point density, and are overlain behind the scatter plots. Hot colors demarcate areas with higher data density. (For interpretation of the references to colour in this figure legend, the reader is referred to the web version of this article.)

population. Straight channel segments exhibit the least amount of data spread, with the highest density of data occurring near the upper symmetrical channel threshold (0.55). Low sinuous channel bends exhibit the most asymmetry variability downslope of the bend apex; conversely, high sinuous channel bends exhibit the most spread in the data upslope of the bend apex. The derived equations from the defined best-fit curves (Fig. 7D—F) can be utilized to infer channel cross-sectional morphology, relative to bend apexes, for stratigraphic models of deep-water slope deposits in which gross planform shape is adequately defined (e.g., in 3-D seismic time slices).

5.6. Cross-sectional asymmetry vs. planform sinuosity

Based on information from the stratigraphic record, it has been shown that, in general, symmetrical channel cross-sections occur

within straighter channel segments (Pyles et al., 2010; Macauley and Hubbard, 2013), which is consistent with the LCCS dataset (Fig. 8). At the threshold between straight to low sinuosity channel bends, cross-sectional asymmetries increase significantly, suggesting any deviation from straight channel trajectories promotes the development of asymmetrical channel morphologies (blue to red in Fig. 8). In contrast, as channels traverse to higher sinuosity channel bends, cross-sectional asymmetries increase by a relatively lower magnitude (red to green in Fig. 8). It is hypothesized that this increase would reach a maximum asymmetry value and remain relatively constant with increasing sinuosities. This positive relationship with respect to increasing sinuosities is also observed in both histograms and scatter plots (Figs. 6 and 7). However, this relationship towards a maximum asymmetry value cannot be fully quantified as a result of limited data in the higher sinuous bend populations. A one-way ANOVA analysis was computed to compare
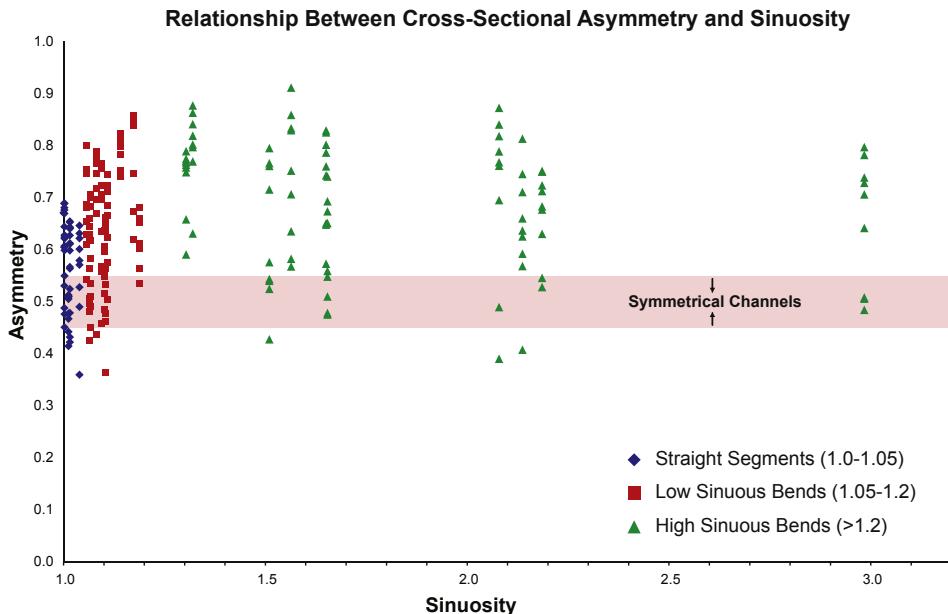
Fig. 8. Cross-sectional asymmetry values versus channel bend sinuosity illustrating the positive relationship, where asymmetry values are proportional to the magnitude of sinuosity. Point-sets are grouped based off their measured sinuosities. The greatest magnitude of change in cross-sectional asymmetry with respect to sinuosity occurs at the transition from straight to low sinuous channel bends. Asymmetry values appear to increase by a lesser degree between low and high sinuous channel bend populations.

the effect of sinuosity on cross-sectional channel asymmetry in submarine channels. The statistical significance test indicates sinuosity does have an effect on cross-sectional channel asymmetry at a p < 0.05 level for the three sinuosity populations (e.g., straight, low and high) $[F(2,240) = 19.81, p = 1.08E-08]$. This analysis corroborates previous findings that cross-sectional asymmetry is indeed proportional to the magnitude of sinuosity (e.g., Peakall et al., 2000; Abreu et al., 2003; Pyles et al., 2010; McHargue et al., 2011), but the magnitude of change in cross-sectional asymmetry with respect to sinuosity is the greatest at the transition from straight to low sinuous channel bends.

6. Application: Tres Pasos Formation outcrop analog

Two outcrop locations, Puma Picana Confluence (PPC) and Puma Picana Confluence North (PPCN), exposed in the Ultima Esperanza District of southern Chile, offer exceptional exposure of a deep-water sinuous slope channel system in the Upper Cretaceous Tres Pasos Formation (Fig. 9); however, these outcrops are separated by over 1 km of limited to absent exposure. Bed-scale facies characterization, mapping of stratigraphic architecture, and paleoflow analysis at each outcrop indicates the strata are part of a sinuous submarine channel system (Fig. 9). The sinuous planform of seven distinct channel bodies is extrapolated based on outcrop data. Applying the sinuous channel morphometrics derived from the Lucia Chica Channel System to the interpreted channel planforms, a 3-D architectural model of the strata is produced, connecting the two outcrop locations. The quantified asymmetry relationships produced inform reconstruction of geologically realistic 3-D surfaces, which are the basis for accurate architectural models of sinuous deep-water channelized systems constructed with data-limited datasets.

6.1. Outcrop context

The ancient deep-water succession in southern Chile was deposited within the Magallanes retroarc foreland basin, which

formed in response to Andean orogenesis during the Late Cretaceous (Wilson, 1991; Fildani et al., 2003; Fildani and Hessler, 2005; Fosdick et al., 2011). The foredeep succession includes >4000 m of deep-water sedimentary strata that were deposited over ~20 Myr (Katz, 1963; Romans et al., 2010; Bernhardt et al., 2012). The final stage of deep-marine basin infill is recorded by the southward progradation of high relief (>1000 m) clinoform systems (Hubbard et al., 2010). These systems filled the basin axially and consist of the analyzed deep-water slope deposits of the Tres Pasos Formation (Hubbard et al., 2010; Schwartz and Graham, 2015; Pemberton et al., 2016). Paleoflow during deposition of the deep-water Tres Pasos Formation was due south on average, parallel to the axis of the foreland basin (Shultz et al., 2005; Romans et al., 2009; Hubbard et al., 2010; Macauley and Hubbard, 2013).

The PPC outcrop consists of 50–55 m of slope channel strata exposed on modern erosional valley walls along the Arroyo Picana; outcrop exposures provide 3-D context (Fig. 9B). The PPCN outcrop (~50 m thick) is exposed along a 2-D outcrop face on a tributary to Arroyo Picana approximately 1 km north of PPC (Fig. 9C). Collectively, the two outcrops are approximately 25 km from the mapped paleoshelf-edge (Hubbard et al., 2010). Traditional field methods including stratigraphic sections and photomosaic interpretations, coupled with high-resolution (5–10 cm) differential GPS surveying, fostered the documentation of detailed sedimentology and stratigraphic architecture. In addition, paleoflow indicators were measured from sole marks, ripples, and imbricated clasts to help constrain the planform expression of the slope channel system. Paleocurrent measurements average 240° at PPC and 175° at PPCN, which reflects the sinuous nature of the studied channel system (Fig. 9B, C).

Both outcrops expose two distinct channelization phases. An early phase is dominated by stratified conglomerate and coarse-grained sandstone over a belt at least 600 m wide. This basal unit is 17 m thick and displays a highly varied internal architecture with a high degree of bed and sedimentary body amalgamation (Fig. 10). It is interpreted as a disorganized channel complex that resulted from numerous channel avulsions (cf. Deptuck et al., 2003;
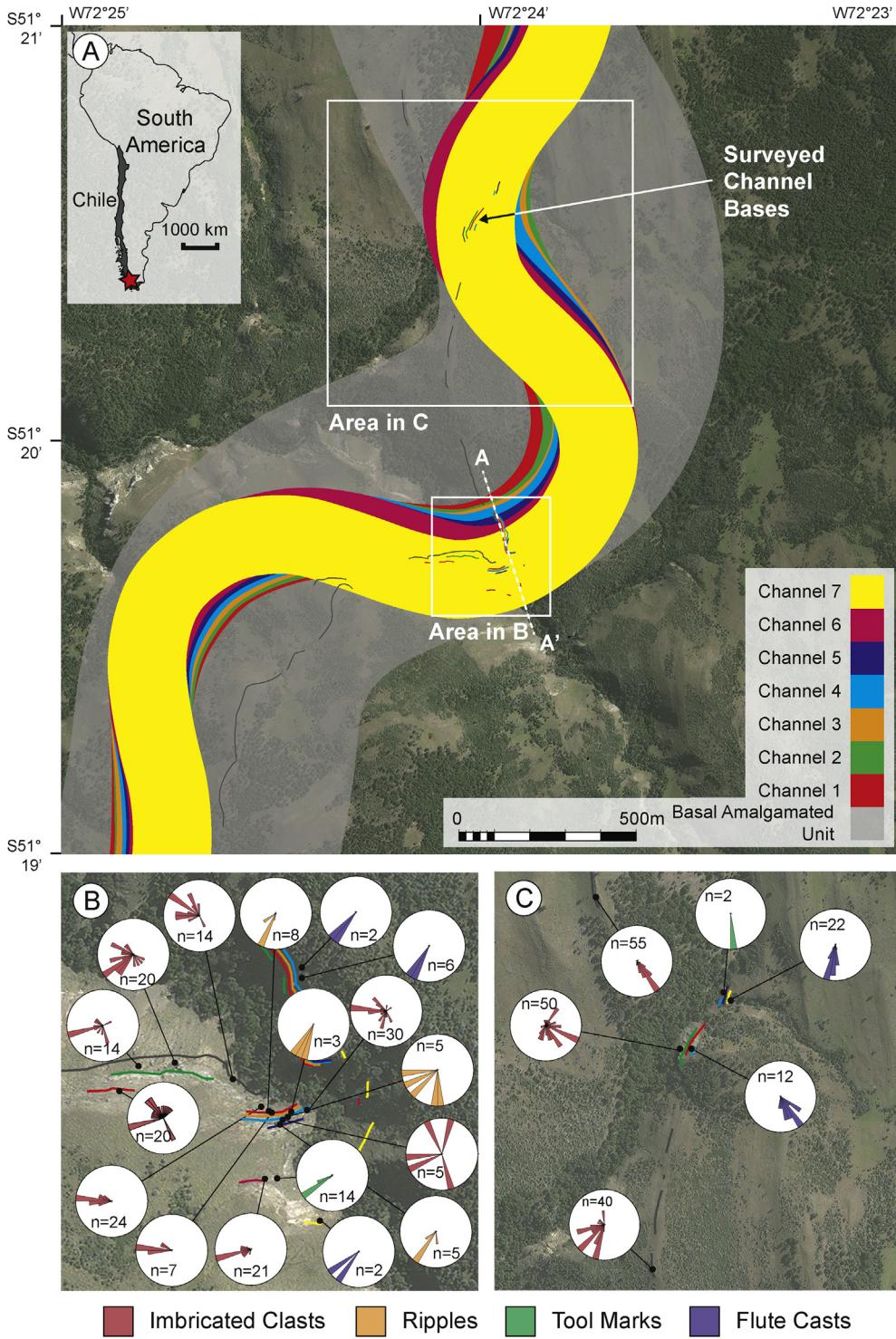
Fig. 9. (A) Interpreted reconstruction of seven vertically stacked sinuous channel fills overlain on a satellite image, based on data collected at PPC (Part B) and PPCN (Part C) (Map data: Google, Digital Globe). These data include facies transitions, stratigraphic stacking of channel bodies and paleoflow measurement. Cross-section A–A' shown in Fig. 10. (B) Close-up image of PPC, and (C) PPCN highlighting the surfaces surveyed (colored lines) and paleoflow rose diagram locations (Map data: Google, Digital Globe).

Hodgson et al., 2011; McHargue et al., 2011; Bain and Hubbard, 2016). The second phase, which is the focus of this study, consists of seven distinct slope channel fills that are estimated to be ~220 m wide on average (Fig. 10). The channel fills are demarcated by characteristics defined by numerous authors, including Mutti and Normark (1987), Pyles et al. (2010), and Hubbard et al. (2014). These channel fills are 8–11 m thick, characterized by asymmetrical cross-sectional fill pattern and architecture, and are aggradational in nature. Collectively, they comprise an organized channel complex (cf. Campion et al., 2000; Sprague et al., 2002; Beaubouef, 2004) that was correlated between the two outcrops, with each of the seven channel fills identified at both locations.
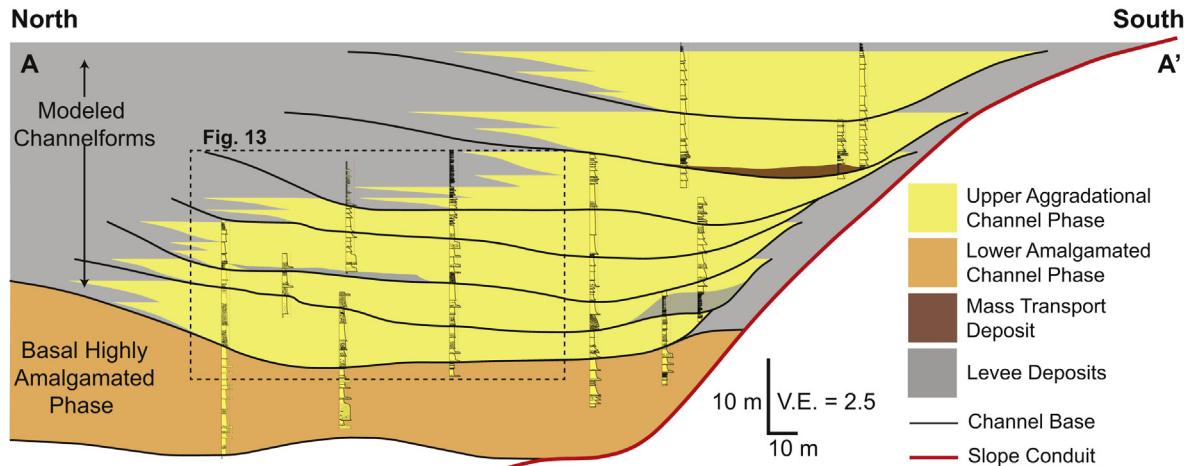
Fig. 10. Strike-oriented cross-section (A—A′) of the approximately 55 m thick deep-water succession exposed at PPC. The lower amalgamated channel phase (orange) is characterized by numerous channel fills that exhibit a highly varied internal architecture with a high degree of bed and sedimentary body amalgamation. It is interpreted as a disorganized channel complex that resulted from numerous channel avulsions. The upper aggradational phase (this study) consists of a series of seven distinct slope channel fills that are estimated to be ~220 m wide. Channel fills are more aggradational in nature; are characterized by asymmetrical cross-sectional fill pattern and architecture; and comprise an organized channel complex. Cross-section location is shown on Fig. 9. (For interpretation of the references to colour in this figure legend, the reader is referred to the web version of this article.)

6.2. Model construction

High-resolution field mapping of channelform surfaces was performed using differential GPS surveying and augmented with bed-scale characterization of internal fill facies and stratigraphic relationships. These observations, coupled with paleoflow measurements, facilitated the reconstruction of planform projections of each channel fill between and beyond the two outcrop locations (Fig. 9A). Inflection points between channel bends were selected for each of the seven channel fills. The defined channel bends were isolated and translated to a reference origin, rotated to a horizontal position and apexes determined (Fig. 3). Sinuosities were subsequently calculated along with the normalized distances up- and down-slope from the bend apexes. Using the quantified relationship defined by the 2nd degree polynomial curves capturing the degree of channel asymmetry versus the normalized distance away from the bend apex (Fig. 7D—E), channel cross-sectional asymmetries were calculated around each bend. For this calculation, three derived equations from the scatter plots were utilized to predict the degree of channel asymmetry for (1) straight segments, (2) low sinuosity bends, and (3) high sinuosity channel bends.

The channelform surfaces were constructed in 3-D modeling software using two point-sets: (1) the interpreted channel edges based on the mapped planform reconstructions; and (2) the calculated thalweg position along the entire channel length based on the relationships defined by the morphometric analysis of the LCCS. The thalweg position for each bend is the product of the calculated asymmetry value at a given geographical location around the bend and the channel width. This value defines the magnitude of the vector normal to the inner margin of the bend to the thalweg position (D_t) (Eq. (1)). Thalweg positions were calculated every 20 m and incorporated into a single line that defines the thalweg along the entire length of the channel, intersecting the two outcrop locations at accurate positions based on field observations. Subsequently, the vertical distance from the thalweg to the top of the channel fill was derived from measured stratigraphic sections (Fig. 10). The two defined point-sets were then interpolated to construct channelform surfaces.

6.3. Model results

6.3.1. Planform thalweg lines

To qualitatively investigate and test the validity of the thalweg line generation workflow for prediction of the thalweg location around a sinuous bend, a thalweg line was calculated for a: (1) sinuous channel interpreted from the Chilean outcrop (Fig. 11A); and (2) two high sinuosity channel bend examples from the modern Y channel system on the western Niger Delta slope (Fig. 11B; Jobe et al., 2015). For the ancient Chilean channel, box-and-whisker plots of measured asymmetry values from the LCCS analysis were scaled to the outcropping channel width (220 m) and positioned with respect to the 9 measured cross-section populations (cf. Fig. 3). As expected, the generated thalweg line for the ancient Chilean system predicts a thalweg position more proximal to the outer edge of the channel near the bend apex, and a thalweg position more proximal to the channel centerline at inflection points. The line predicts normal asymmetrical channel cross-sections occur around channel bends with more symmetrical channel cross-sections near the inflection points, consistent with observations from the LCCS analysis.

Calculated thalweg lines generated solely from channel planform information for the two high sinuosity channel bend examples in the Niger Delta slope are illustrated in Fig. 11B. In both examples the calculated line predicts a thalweg position proximal to the outer bend margin around the bend, similar to the natural thalweg pathway in both bends. In the most upslope bend (Fig. 11B; sinuosity 1.3) the calculated line overestimates the thalweg position up to a maximum of 35 m towards the outer bend margin (19% difference versus the average channel width), with the largest discrepancy occurring near the bend apex. The second bend (sinuosity 1.5) exhibits the greatest discrepancy between the calculated and natural thalweg lines near to the upslope inflection point (Fig. 11B). At this location, the natural thalweg line takes an atypical trajectory towards the inner margin before ultimately transitioning towards the outer margin. The calculated line underestimates the thalweg position by a maximum of 25 m (9% difference), again near the bend apex; however, the natural and calculated lines closely correlate to one another downslope of the bend apex before transitioning into the successive bend. The differences in the calculated
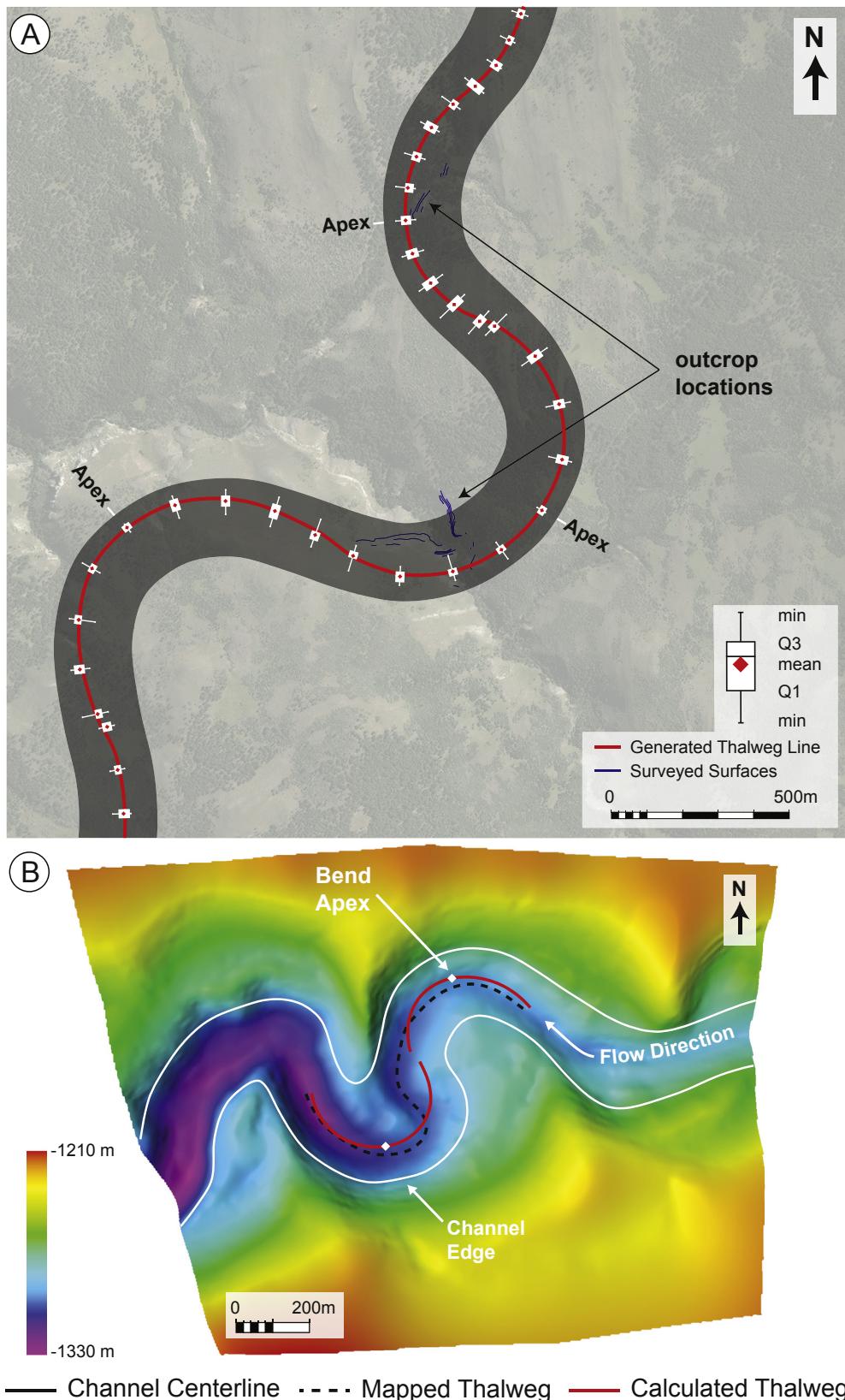
Fig. 11. Generated thalweg lines using the calculated channel asymmetries based on the normalized distances away from the bend apexes. (A) Generated thalweg line correlates with the median asymmetry values for each cross-section position along the channel bend from the Chilean outcrop (Map data: Google, Digital Globe. (B) Calculated and mapped thalweg lines generated for two high sinuosity channel bends from the Niger Delta slope (modified from Jobe et al., 2015).

and natural thalweg lines may be influenced by the changes in sediment routing and flux within the Nigerian system (cf. Jobe

et al., 2015). The bathymetric surface morphology is a product of a channel system that was abandoned during the Late Pleistocene (~130 ka), which subsequently captured a smaller channel system upslope (~50 ka). The re-occupation of the channel system with smaller, underfit flows resulted in variable sedimentation in the channel on both outer and inner channel bends (cf. Jobe et al., 2015). Despite geomorphic modifications by underfit flows, the analysis shows the thalweg line generation methodology is able to predict the thalweg position in a natural slope channel system. One assumption for the developed workflow is that channel widths remain close to constant around a sinuous bend, which is not always the case in natural systems (Fig. 11B; Babonneau et al., 2002; Jobe et al., 2015); however, if the channel width does not change significantly, the average width around a bend can substitute for the actual channel width to predict the thalweg position, as shown in the Nigerian slope channel bend examples.

6.3.2. Channel morphology and stacking pattern

The interpolated channelforms from the outcrop analysis are broad with thalweg widths ranging from 10 to 20 m. Channel surfaces exhibit steeper slopes on the outer bank with the inner bank characterized by a more gradual slope towards the thalweg around sinuous bends (Fig. 12). These morphological characteristics are comparable with channelform surfaces observed in the LCCS dataset and consistent with outcrop observations (Fig. 13). In addition, generated channel surfaces exhibit symmetrical channel cross-sections at the inflection points between two successive channel bends (Fig. 12).

From the outcrop, lithologies and stratigraphic relationships

indicate that channelforms systematically step (lateral and vertical offset) towards outer channel bends (Fig. 10). This stratigraphic relationship is captured in the architectural surface model (Fig. 12). Lateral stacking relationships of slope channels, such as those observed in Chile, have been documented in numerous outcrop exposures (Clark and Pickering, 1996; Campion et al., 2005; O'Byrne et al., 2007; Hodgson et al., 2011; Khan and Arnott, 2011; Pyles et al., 2010; Jobe et al., 2010; Di Celma et al., 2011; Moody et al., 2012), as well as seismically imaged systems (Posamentier and Kolla, 2003; Deptuck et al., 2003; Mayall et al., 2006; Babonneau et al., 2010; Kolla et al., 2012). This stacking relationship is linked to the systematic lateral sinuous bend expansion (swing) and downslope translation (sweep) of successive channels (cf. Peakall et al., 2000).

7. Discussion

7.1. Geomorphic vs. stratigraphic surfaces

Analysis of the Earth's surface offers the opportunity to quantify geomorphic features (Mutti and Normark, 1987; Clark and Pickering, 1996; Babonneau et al., 2010; Sylvester et al., 2012; Maier et al., 2012; Jobe et al., 2015); however, geomorphic surfaces are commonly not fully preserved in the rock record as a result of protracted processes of erosion and deposition (Pemberton et al., 2016). In contrast, stratigraphic surfaces, including channelforms, capture a wide range of temporal scales. These surfaces are typically diachronous, sculpted on the seafloor by innumerable erosive and depositional events (cf. Strong and
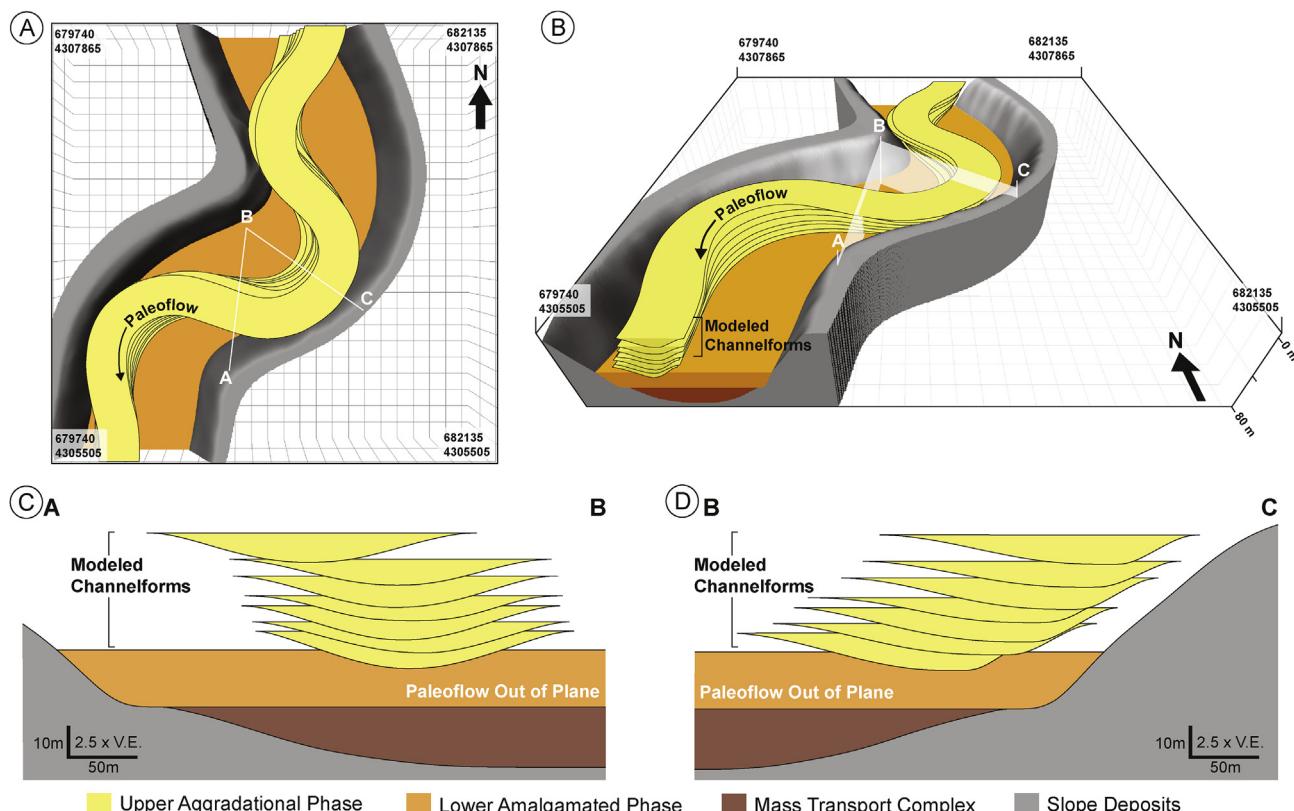
Fig. 12. Generated architectural model of the outcropping Chilean deep-water slope channel system. The yellow sinuous channel fills are the focus of this analysis. (A) Planform perspective of the architectural model. (B) Perspective image of the architectural model looking upslope. (C) Strike-cross section at the inflection point between two successive bends showing the generated symmetrical cross-sectional channelforms constrained from the LCCS morphometric data. (D) Strike cross-section at the apex of a high sinuous channel bend illustrating the generated asymmetrical channelforms. (For interpretation of the references to colour in this figure legend, the reader is referred to the web version of this article.)
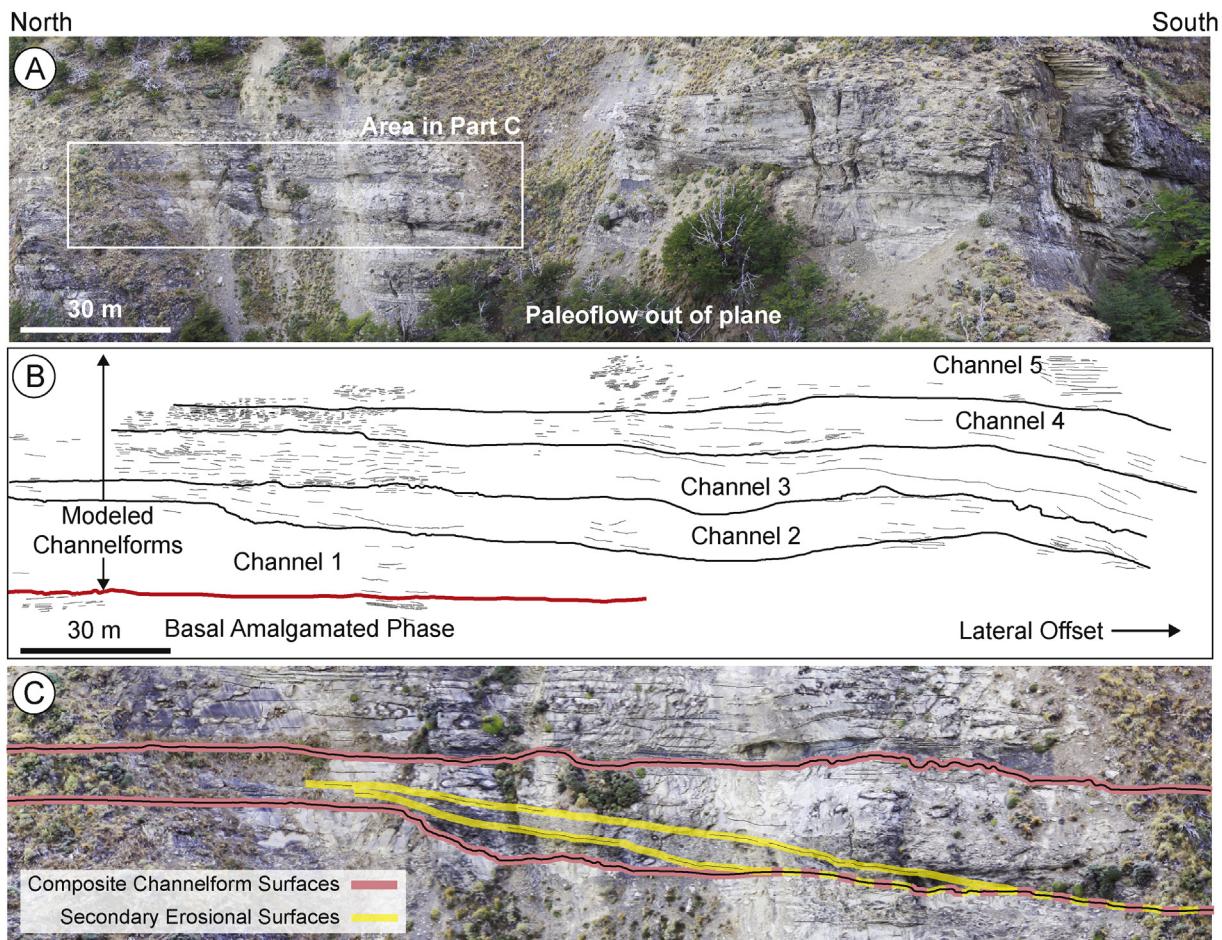
Fig. 13. (A) Overview photomosaic of the strike orientated outcrop at PPC. Photo location shown in Fig. 10(B) Line-drawing trace of stacked slope channel deposits at PPC. The stratigraphic succession is characterized by a series of asymmetrical channelform bodies, shifting progressively and systematically southward. (C) Enlarged photo illustrating several erosional surfaces that downlap onto the channel base, generating a highly composite surface that formed over the channel lifecycle.

Paola, 2008; Conway et al., 2012; Sylvester et al., 2012; Hubbard et al., 2014). Sheets et al. (2008) used scaled-down physical experiments to demonstrate that alluvial channel bodies and their associated stratigraphic surfaces were larger in cross-sectional geometry than the channels that formed them. However, the preserved stratigraphic surfaces shared similar geometrical artifacts with their geomorphic counterparts (e.g., width to depth/thickness ratio). Therefore, despite the fact that geomorphic surfaces are typically not entirely preserved in the rock record, their morphology is partially recorded in the stratigraphic product. This has important implications for the utility of seafloor surfaces in the interpretation of the stratigraphic record, as has been undertaken in this study.

Numerous stages of erosion result in outcropping channel base surfaces that exhibit slightly rugose to smooth profiles; locally, distinct steps, or notches are present (e.g., Hubbard et al., 2014). Likewise, channel base morphologies from LCCS occasionally exhibit stepped or terraced margins on the inner bank (Maier et al., 2012, 2013). These terraced surfaces are interpreted to have generated through progressive erosion, channel migration and meander development as the sinuous system evolved (e.g., Babonneau et al., 2010; Hubbard et al., 2014; Jobe et al., 2015). At the outcrop, several intra-channel erosion surfaces that merge or downlap onto primary basal channelform surfaces, contribute to the generation of a highly composite stratigraphic surface (Fig. 13).

A comparison of the modeled channelform from the Lucia Chica

analysis and stratigraphic surfaces from the Tres Pasos Formation informs the limitations of the analysis. A notable limitation of the comparison is that channel fills are not entirely preserved in the outcrop and instead asymmetry is largely interpreted from internal lithofacies and stratigraphic stacking patterns. Overall, the interpreted cross-sectional area of the organized, aggradational channel complex in the vicinity of PPC is 7275 m^2 (Fig. 10); the LCCS-based model measures 6206 m^2 (Fig. 12D). The difference between the two strike cross sections is 1070 m^2 (16%) with the greatest discrepancy at the outer margin of the channelized bodies. The model underestimates the cross sectional area, or more importantly the three-dimensional volume of the modeled slope channel fills. This is inferred to be a direct result of the protracted development of stratigraphic surfaces, which are sculpted by multiple phases of erosion and deposition during the channel lifecycle (e.g., Sheets et al., 2008; Hubbard et al., 2014).

7.2. Formative channel processes

Turbulent density currents that form and maintain submarine channels contain secondary flows, which influence cross-sectional channel morphologies (cf. Corney et al., 2006; Keevil et al., 2006; Peakall et al., 2007; Peakall and Sumner, 2015). These flows form a characteristic helical spiral motion, similar to flows observed in their fluvial counterparts (Thorne et al., 1985), resulting from pressure forces associated with super-elevation of the denser,

sediment-laden fluid towards the outer bank (cf. Corney et al., 2006; Keevil et al., 2006; Peakall and Sumner, 2015). Secondary flows are expected to occur within, straight, low, and high sinuous submarine channel bends, and have been documented in physical and numerical models (Kassem and Imran, 2004; Corney et al., 2006; Keevil et al., 2006; Huang et al., 2012; Janocko et al., 2013b), as well as in active lacustrine systems (Wei et al., 2013) and saline density-current driven channels (Parsons et al., 2010; Sumner et al., 2014). Secondary flows can be normal or reverse depending on flow parameters (Corney et al., 2006; Keevil et al., 2006; Peakall et al., 2007; Corney et al., 2008; Peakall and Sumner, 2015); reverse secondary flows are represented by a helical motion in which the basal flow is directed towards the outer bank at the bend apex (Fig. 14A, B; Corney et al., 2006; Keevil et al., 2007), whereas normal secondary flows exist when the basal flow is orientated towards the inner margin at the bend apex (Fig. 14A, B; Kassem and Imran, 2004; Imran et al., 2007).

Experimental results of secondary flow cells, reverse or normal, suggest the outer margin of a channel bend is exposed to considerably higher shear stress then the inner margin, contributing to enhanced erosion along the outer margin of a bend (Fig. 14A) (cf. Corney et al., 2006; Keevil et al., 2006; Peakall et al., 2007; Amos et al., 2010). Enhanced erosion sculpts asymmetrical channel cross-sections around the bend and proximal to the apex (Fig. 5A), consistent with the LCCS (populations 3−7; Fig. 14C). Although experimental work has suggested higher outer bend erosion is concentrated downstream of a bend apex (Amos et al., 2010; Straub et al., 2011), our channel asymmetry measurements do not apparently validate this hypothesis (Fig. 7). Keevil et al. (2006) suggests that the overall strength of these secondary flow cells increase as a function of sinuosity, which most likely contributes to the overall higher cross-sectional asymmetry values in the higher sinuosity bend populations. Through time, enhanced erosion along outer channel margins promotes bend expansion, leading to an increase
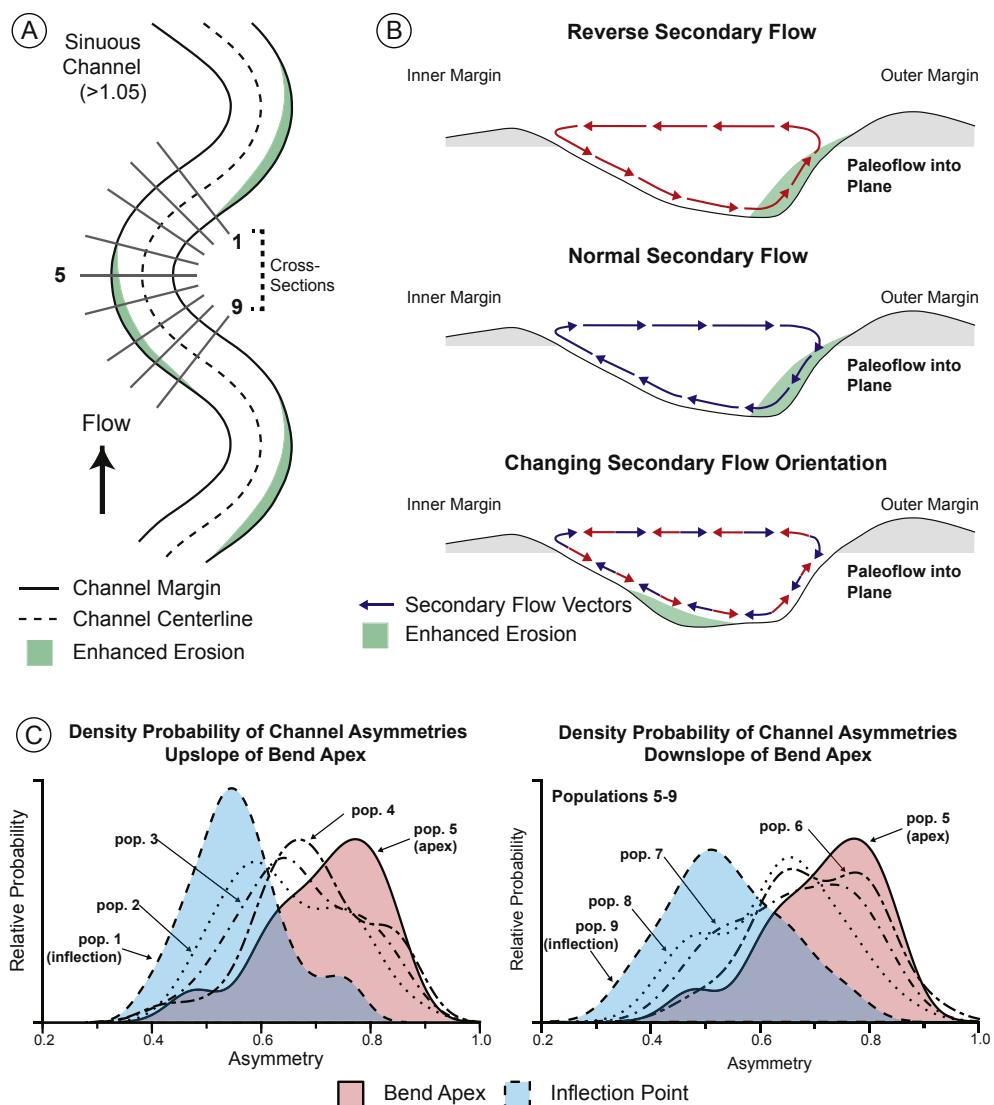
Fig. 14. (A) A generalized model for a sinuous submarine channel based on physical density flow experiments. Areas of enhanced erosion around a sinuous bend highlighted by green areas (modified from Amos et al., 2010). Cross-sectional groups are shown by grey lines. (B) Schematic diagrams showing reverse and normal secondary flow fields at the bend apex of a sinuous submarine channel (cross-section 5 in Part A). Cross-sections are looking downstream. Reverse flow is characterized by a basal outward flow vector at the bend apex. Normal flows represent a basal inward directed flow vector at the bend apex. When secondary flow cells change orientation, erosion is enhanced along the inner margin. (C) Density probability plots of channel morphologies upslope and downslope of the bend apex from the LCCS analysis. Asymmetrical channels are encountered proximal to the apex (population 5) with symmetrical channels near the inflection point (population 1 and 9). (For interpretation of the references to colour in this figure legend, the reader is referred to the web version of this article.)

in sinuosity (cf. Peakall et al., 2000; Posamentier and Kolla, 2003; Pyles et al., 2010). Conversely, at inflection points, secondary flows exhibit more uniform helical profiles focused around the channel centerline, suggesting limited shear stress along one specific margin (cf. Keevil et al., 2006). This condition most likely contributes to the more symmetrical channel cross-sections encountered at the inflection points (populations 1 and 9; Fig. 14C).

In straight channels, multiple secondary helical cells are the dominant process that influences cross-sectional geometries (cf. Peakall and Sumner, 2015). These multiple cells can be caused by anisotropy in turbulent fluctuations, oblique to the main flow (McLelland et al., 1999; Albayrak and Lemmin, 2011). Although, multiple helical cells have only been documented in fluvial experiments of straight channels, it is postulated that they would generate conditions where shear stress is not focused along one specific margin in a submarine channel, in contrast to sinuous channel bends; overall they generate more symmetrical channel cross-sections (Fig. 5B), consistent with the more frequent symmetrical channelforms encountered within straighter channel populations from the LCCS.

Secondary flow cells can change orientations from normal to reverse as a result of temporal and spatial changes within the flow including, but not limited to: loss of flow confinement and overspill (Dorrell et al., 2013), and waning of the flow as it evolves through time (Giorgio Serchi et al., 2011). Based on conceptual fluid dynamics models, the change in helical polarity is postulated to force the migration of the high velocity core of the main downslope flow to towards the inner margin (Giorgio Serchi et al., 2011). If flow orientation changes are prolonged, shear stress would perhaps have a significant impact along the inner margin, facilitating enhanced erosion and potentially aiding in the sculpting of inverse asymmetrical channel morphologies (Figs. 5 and 14B). In the LCCS dataset, these channelforms more frequently occur near the downslope inflection point, potentially related to flow overspill around the bend.

7.3. Reservoir prediction implications

Reservoir connectivity is strongly dependent on channel sinuosity and stacking patterns. In more sinuous channel fill successions, connectivity is controlled by the position of thalweg deposits and the amount of incision with respect to the underlying channel fill, impacting the vertical and lateral connectivity of reservoir quality facies (Barton et al., 2010; Di Celma et al., 2011; Funk et al., 2012; Jackson, 2014). Further impacting reservoir connectivity is aggradation rate and the associated stacking pattern of successive channel fill sequences (cf. Mayall and O'Byrne, 2002; Abreu et al., 2003; Mayall et. 2006; Cross et al., 2009; Funk et al., 2012). If the amount of aggradation is less than the underlying channel fill thickness, with minimal lateral offset, channel fills have an increased likelihood of being connected in 3-D space. Pyles et al. (2010) document highest geobody connectivity in straighter channel segments, which exhibit symmetrical channel morphologies that vertically aggrade. Conversely, reservoir connectivity is lowest associated with asymmetrical channel cross-sectional geometries, where channel fills laterally offset successive bodies, driven by sinuous bend expansion and translation (cf. Peakall et al., 2000; Posamentier and Kolla, 2003; Pyles et al., 2010). Therefore, recognizing and accurately predicting channel stacking patterns, as well as cross-sectional morphologies, is important to mitigate risk associated with reservoir compartmentalization (Mayall and O'Byrne, 2002; Mayall et al., 2006).

The application of the methodology and morphometric analysis presented in this study can be used as a tool to bridge the gap between 1-D borehole and 3-D seismic reflection data, aimed at building more predictive models of channel connectivity. Planform geometries or channel centerlines roughly interpreted from seismic (e.g., deep-water channels offshore west Africa; Abreu et al., 2003; Deptuck et al., 2003, 2007; Mayall et al., 2006; Cross et al., 2009; Jobe et al., 2015) combined with the equations presented herein can be leveraged to generate realistic channelform surfaces. This methodology is a deterministic approach where cross-sectional channel asymmetries are predicted based on the best-fit equations for multiple channel bends from the LCCS dataset. Uncertainty is prevalent in these interpretations as a function of the limitations of resolution and incomplete subsurface sampling from wireline logs, drill cores or seismic reflection data. To capture the range of uncertainty associated with hydrocarbon volumes and connectivity of reservoir units, the workflow could be repeated for several stochastic simulations of possible channel centerline scenarios (e.g., centerline prediction from event-based modeling workflows; Pyrcz et al., 2015 and references therein). Each centerline would then serve as the basis to stochastically assigned planform extents and cross-sectional asymmetries constrained by the range of statistical variation presented from the LCCS dataset and a distribution of probable channel widths. Both methods would generate several reservoir models that could subsequently be used to better constrain the uncertainty of initial reservoir volumes and net pay connectivity from channel to channel.

8. Conclusions

The results of this study inform a range of slope channel morphologies and the geomorphic relationship between planform morphology and cross-sectional asymmetry in sinuous submarine channel systems. Three channel morphologies, normal asymmetric, symmetric, and inverse asymmetric, are classified based on the location of the thalweg with respect to the inner bend margin. This analysis documents that straight channel segments (sinuosities 1.0—1.05) exhibit the most symmetrical cross-sectional morphologies, with higher cross-sectional asymmetry values occurring in more sinuous channel bend populations. Low (sinuosities 1.05—1.2) and high sinuosity (sinuosities >1.2) channel bends exhibit maximum cross-sectional asymmetries at the bend apex, with the most symmetrical morphologies occurring at the inflection points between two successive bends. Altogether, asymmetry values progressively increase within each increasing sinuosity population, highlighting that cross-sectional asymmetry is proportional to the magnitude of sinuosity. The magnitude of change in cross-sectional asymmetry with respect to sinuosity is the greatest at the transition from straight to low sinuous channel bends, and it appears to increase by a lesser degree between the low to high sinuous channel bend populations. The quantified relationships are used to condition an architectural model based on a sinuous slope channel complex (Cretaceous Tres Pasos Formation) deposit sporadically exposed in outcrops of southern Chile. The application of the methodology derived from morphometric analysis can be used to build more geologically accurate reservoir models, improve predictions of reservoir architecture and flow connectivity, and bridge the resolution gap between 1-D borehole and 3-D seismic reflection datasets in the subsurface.

References

Abreu, V., Sullivan, M., Pirmez, C., Mohrig, D., 2003. Lateral accretion packages (LAPs): an important reservoir element in deep water sinuous channels. Mar. Petroleum Geol. 20, 631—648.

Albayrak, I., Lemmin, U., 2011. Secondary currents and corresponding surface velocity patterns in a turbulent open-channel flow over a rough bed. J. Hydraul. Eng. 137, 1318—1334.

Alves, T.M., 2010. 3D seismic examples of differential compaction in mass transport deposits and their effect on post-failure strata. Mar. Geol. 271, 212—224.

Amos, K.J., Peakall, J., Bradbury, P.W., Roberts, M., Keevil, G., Gupta, S., 2010. The influence of bend amplitude and planform morphology on flow and sedimentation in submarine channels. Mar. Petroleum Geol. 27, 1431—1447.

Babonneau, N., Savoye, B., Cremer, M., Klein, B., 2002. Morphology and architecture of the present canyon and channel system of the Zaire Deep-Sea Fan. Mar. Petroleum Geol. 19, 445—467.

Babonneau, N., Savoye, B., Cremer, M., Bez, M., 2010. Sedimentary architecture in meanders of a submarine channel: detailed study of the present Congo turbidite channel (Zaiango Project). J. Sediment. Res. 80, 852—866.

Bain, H.A., Hubbard, S.M., 2016. Stratigraphic evolution of a long-lived channel system in the Late Cretaceous Nanaimo Group, British Columbia, Canada. Sediment. Geol. 337, 113—132.

Barton, M., O'Byrne, C., Pirmez, C., Prather, B., van der Vlugt, F., Alpak, F.O., Sylvester, Z., 2010. Turbidite channel architecture: recognizing and quantifying the distribution of channel-base drapes using core and dipmeter data. In: Poppelreiter, M., Garcıa-Carballido, C., Kraaijveld, M. (Eds.), Dipmeter and Borehole Image Log Technology, Memoir 92. AAPG, pp. 195—210.

Beaubouef, R.T., Rossen, C., Zelt, F.B., Sullivan, M.D., Mohrig, D.C., Jennette, D.C., 2000. Deepwater sandstones, Brushy Canyon Formation, west Texas. AAPG Continuing Education Course Note Series, no. 40. In: Field Guide for American Association of Petroleum Geologists Hedberg Field Research Conference, April 15—20, 1999, p. 48.

Beaubouef, R.T., 2004. Deep-water leveed-channel complexes of the Cero Toro formations, Upper Cretaceous, southern Chile. AAPG Bull. 88, 1471—1500.

Bernhardt, A., Jobe, Z.R., Grove, M., Lowe, D.R., 2012. Paleogeography and diachronous infill of an ancient deep-marine foreland basin, Upper Cretaceous Cerro Toro Formation, Magallanes Basin. Basin Res. 23, 1—26.

Brice, J.C., 1974. Evolution of meander loops. GSA Bull. 85, 581—586.

Campion, K.M., Sprague, A.R., Mohrig, D., Lovell, R.W., Drzewiecki, P.A., Sullivan, M.D., Ardill, J.A., Jensen, G.N., Sickafoose, D.K., 2000. Outcrop expression of confined channel complexes. In: Weimer, P., Slatt, R.M., Coleman, J., Rosen, N.C., Nelson, H., Bouma, A.H., Styzen, M.J., Lawrence, D.T. (Eds.), Deepwater Reservoirs of the World. CSSEPM Foundation 20th Annual Research Conference, pp. 127—150.

Campion, K.M., Sprague, A.R., Sullivan, M.D., 2005. Architecture and lithofacies of the Capistrano Formation (Miocene—Pliocene), San Clemente, California. In: Pacific Section of the SEPM, Annual Fall Fieldtrip Guidebook, October 29, 2005, p. 42.

Catterall, V., Redfern, J., Gawthorpe, R., Hansen, D., Thomas, M., 2010. Architectural style and quantification of a submarine channel—levee system located in a structurally complex area: offshore Nile Delta. J. Sediment. Res. 80, 991—1017.

Clark, J.D., Kenyon, N.H., Pickering, K.T., 1992. Quantitative analysis of the geometry of submarine channels: implications for the classification of submarine fans. Geology 20, 633—636.

Clark, J.D., Pickering, K.T., 1996. Architectural elements and growth patterns of submarine channels: application to hydrocarbon exploration. AAPG Bull. 80, 194—220.

Conway, K., Barrie, J., Picard, K., Bornhold, B., 2012. Submarine channel evolution: active channels in fjords, British Columbia, Canada. Geo-Marine Lett. 32, 301—312.

Corney, R.K.T., Peakall, J., Parsons, D.R., Elliott, L., Amos, K.J., Best, J.L., Keevil, G.M., Ingham, D.B., 2006. The orientation of helical flow in curved channels. Sedimentology 53, 249—257.

Corney, R.K.T., Peakall, J., Parsons, D.R., Elliot, L., Best, J.L., Thomas, R.E., Keevil, G.M., Ingham, D.B., Amos, K.J., 2008. Reply to discussion of Imran et al. on "The orientation of helical flow in curved channels" by Corney, et al. Sedimentology

53, 249—257. Sedimentology 55, 241—247.

Covault, J.B., Shelef, E., Traer, M., Hubbard, S.M., Romans, B.W., Fildani, A., 2012. Deep-water channel run-out length: insights from seafloor geomorphology. J. Sediment. Res. 82, 21—36.

Covault, J.A., Kostic, S., Paull, C.K., Ryan, H.F., Fildani, A., 2014. Submarine channel initiation, filling and maintenance from sea-floor geomorphology and morphodynamic modeling of cyclic steps. Sedimentology 61, 1031—1054.

Cross, N.E., Cunningham, A., Cook, R.J., Taha, A., Esmaie, E., El Swidan, N., 2009. Three-dimensional seismic geomorphology of a deep-water slope-channel system: the Sequoia field, offshore west Nile Delta, Egypt. AAPG Bull. 93, 1063—1086.

Damuth, J.E., Flood, R.D., 1984. Morphology, sedimentation processes, and growth pattern on the Amazon Deep-Sea Fan. Geo-Marine Lett. 3, 109—117.

De Ruig, M.J., Hubbard, S.M., 2006. Seismic facies and reservoir characteristics of a deep marine axial channel belt in the Molasse Basin, Puchkirchen Formation, Upper Austria. AAPG Bull. 90, 735—752.

Deptuck, M.E., Steffens, G.S., Barton, M., Pirmez, C., 2003. Architecture and evolution of upper fan channel-belts on the Niger Delta slope and in the Arabian Sea. Mar. Petroleum Geol. 20, 649—676.

Deptuck, M.E., Sylvester, Z., Pirmez, C., O'Byrne, C., 2007. Migration-aggradation history and 3-D seismic geomorphology of submarine channels in the Pleistocene Benin-major Canyon, western Niger Delta slope. Mar. Petroleum Geol. 24, 403—433.

Di Celma, C.N., Brunt, R.L., Hodgson, D.M., Flint, S.S., Kavanagh, J.P., 2011. Spatial and temporal evolution of a Permian submarine slope channel-levee system, Karoo Basin, South Africa. J. Sediment. Res. 81, 579—599.

Dixon, B.T., 2003. Slope channel morphology and depositional controls: the Pleistocene-Holocene Niger Delta slope as an analog for ancient slope systems. In: AAPG Annual Convention Abstract 90013, AAPG Annual Convention, 11—14 May, Salt Lake City, Utah.

Dorrell, R.M., Darby, S.E., Peakall, J., Sumner, E.J., Parsons, D.R., Wynn, R.B., 2013. Superelevation and overspill control secondary flow dynamics in submarine channels. J. Geophys. Res. 118, 3895—3915.

Droz, L., Bellaiche, G., 1985. Rhone Deep-Sea Fan: morphostructure and growth pattern. AAPG Bull. 69, 460—479.

Ferry, J.-N., Parize, O., Mulder, T., Raillard, S., 2005. Sedimentary architecture and growth pattern of turbidite systems in distal part of a median fan: example of the Upper Miocene sedimentary sequence of the Lower Congo basin. Geodin. Acta 18, 145—152.

Fildani, A., Cope, T., Graham, S.A., Wooden, J., 2003. Initiation of the Magallanes foreland basin: timing of the southernmost Patagonian Andes orogeny revised by detrital zircon provenance analysis. Geology 31, 1081—1084.

Fildani, A., Hessler, A.M., 2005. Stratigraphic record across a retroarc basin inversion: Rocas Verdes-Magallanes basin, Patagonian Andes, Chile. GSA Bull. 117, 1596—1614.

Fildani, A., Hubbard, S.M., Covault, J.A., Maier, K.L., Romans, B.W., Traer, M., Rowland, J.C., 2013. Erosion at inception of deep-sea channels. Mar. Petroleum Geol. 41, 48—61.

Flood, R.D., Damuth, J.E., 1987. Quantitative characteristics of sinuous distributary channels on the Amazon Deep-Sea Fan. GSA Bull. 98, 728—738.

Fosdick, J.C., Romans, B.W., Fildani, A., Calderon, M.N., Bernhardt, A., Graham, S.A., 2011. Kinematic evolution of the Cretaceous-Neogene Patagonia thrust belt and Magallanes foreland basin, Chile and Argentina (51°30′ S). GSA Bull. 123, 1679—1698.

Funk, J.E., Slatt, R.M., Pyles, D.R., 2012. Quantification of static connectivity between deep-water channels and stratigraphically adjacent architectural elements using outcrop analogs. AAPG Bull. 96, 277—300.

Gee, M.J.R., Gawthorpe, R.L., Friedmann, S.J., 2006. Triggering and evolution of a giant submarine landslide, offshore Angola, revealed by 3D seismic stratigraphy and geomorphology. J. Sediment. Res. 76, 9—19.

Gee, M.J.R., Gawthorpe, R.L., Bakke, K., Friedmann, S.J., 2007. Seismic geomorphology and evolution of submarine channels from the Angolan continental margin. J. Sediment. Res. 77, 433—446.

Giorgio Serchi, F., Peakall, J., Ingham, D.B., Burns, A.D., 2011. A unifying computational fluid dynamics investigation on the river-like to river-reversed secondary circulation in submarine channel bends. J. Geophys. Res. 116, 1—19.

Greene, H.G., Maher, N.M., Paull, C.K., 2002. Physiography of the Monterey Bay National Marine Sanctuary and implications about continental margin development. Mar. Geol. 181, 55—82.

Hickin, E.J., 1974. The development of meanders in natural river channels. Am. J. Sci. 275, 470—478.

Hickin, E.J., Nanson, G.C., 1975. The character of channel on the Beatton River, Northeast British Columbia, Canada. GSA Bull. 86, 487—494.

Hodgson, D.M., Di Celma, C.N., Brunt, R.L., Flint, S.S., 2011. Submarine Slope Degradation and Aggradation and the Stratigraphic Evolution of Channel-levee Systems, vol. 168. Journal of the Geological Society, London, pp. 625—628.

Huang, H., Imran, J., Pirmez, C., 2012. The depositional characteristics of turbidity currents in submarine sinuous channels. Mar. Geol. 329, 93—102.

Hubbard, S.M., Fildani, A., Romans, B.W., Covault, J.A., McHargue, T.R., 2010. High-relief slope clinoform development: insights from outcrop, Magallanes Basin, Chile. J. Sediment. Res. 80, 357—375.

Hubbard, S.M., Covault, J.A., Fildani, A., Romans, B.R., 2014. Sediment transfer and deposition in slope channels: deciphering the record of enigmatic deep-sea processes from outcrop. GSA Bull. 126, 857—871.

Hubscher, C., Spieβ, V., Breitzke, M., Weber, M.E., 1997. The youngest channel—levee

system of the Bengal fan: results from digital sediment echosounder data. Mar. Geol. 141, 125–145.

Hudson, P.F., Kesel, R.H., 2000. Channel migration and meander-bend curvature in the lower Mississippi River prior to major human modification. Geology 28, 531–534.

Imran, J., Islam, M.A., Huang, H., Kassem, A., Dickerson, J., Pirmez, C., Parker, G., 2007. Helical flow couplets in submarine gravity underflows. Geology 35, 659–662.

Jackson, A.A., 2014. Characterizing Static Reservoir Connectivity of Deep-water Slope Deposits Using Detailed Outcrop-based Facies Models, Tres Pasos Formation, Magallanes Basin, Chilean Patagonia. Unpublished MSc thesis. University of Utah.

Janocko, M., Nemec, W., Henriksen, S., Warchol, M., 2013a. The diversity of deep-water sinuous channel belts and slope valley-fill complexes. Mar. Petroleum Geol. 41, 7–34.

Janocko, M., Cartigny, M.B.J., Nemec, W., Hansen, E.W.M., 2013b. Turbidity current hydraulics and sediment deposition in erodible sinuous channels: laboratory experiments and numerical simulations. Mar. Petroleum Geol. 41, 222–249.

Jobe, Z.R., Bernhardt, A., Lowe, D.R., 2010. Facies and architectural asymmetry in a conglomerate-rich submarine channel fill, Cerro Toro Formation, Sierra del Toro, Magallanes basin, Chile. J. Sediment. Res. 80, 1085–1108.

Jobe, Z.R., Sylvester, Z., Parker, A.O., Howes, N., Slowey, N., Pirmez, C., 2015. Rapid adjustment of submarine channel architecture to changes in sediment supply. J. Sediment. Res. 85, 729–753.

Kassem, A., Imran, J., 2004. Three-dimensional modeling of density current. II. Flow in sinuous confined and unconfined channels. J. Hydraul. Res. 42, 591–602.

Kastens, K.A., Shor, A.N., 1986. Evolution of a channel meander on the Mississippi Deep-Sea Fan. AAPG Bull. 71, 165–175.

Katz, H.R., 1963. Revision of Cretaceous stratigraphy in Patagonian Cordillera of Ultima Esperanza, Magallanes Province, Chile. AAPG Bull. 47, 506–524.

Keevil, G.M., Peakall, J., Best, J.L., Amos, K.J., 2006. Flow structure in sinuous submarine channels: velocity and turbulence structure of an experimental submarine channel. Mar. Geol. 229, 241–257.

Keevil, G.M., Peakall, J., Best, J.L., 2007. The influence of scale, slope and channel geometry on the flow dynamics of submarine channels. Mar. Petroleum Geol. 24, 487–503.

Khan, Z.A., Arnott, R.W.C., 2011. Stratal attributes and evolution of asymmetric inner- and outer-bend levee deposits associated with an ancient deep-water channel-levee complex within the Isaac Formation, southern Canada. Mar. Petroleum Geol. 28, 824–842.

Knighton, A.D., 1981. Asymmetry of river channel cross-sections: part I. Quantitative indices. Earth Surf. Process. Landf. 6, 581–588.

Knighton, A.D., 1982. Asymmetry of river channel cross-sections: part II. Mode of development and local variation. Earth Surf. Process. Landf. 7, 117–131.

Kolla, V., Coumes, F., 1987. Morphology, internal structure, seismic stratigraphy and sedimentation of Indus Fan. AAPG Bull. 71, 650–677.

Kolla, V., Bourges, P.H., Urruty, J.M., Safa, P., 2001. Evolution of deep-water Tertiary sinuous channels offshore Angola (west Africa) and implications for reservoir architecture. AAPG Bull. 85, 1373–1405.

Kolla, V., Posamentier, H.W., Wood, L.J., 2007. Deep-water and fluvial sinuous channel – characteristics, similarities and dissimilarities, and modes of formations. Mar. Petroleum Geol. 24, 388–405.

Kolla, V., Bandyopadhyay, A., Gupta, P., Mukherjee, B., Ramana, D.V., 2012. Morphology and internal structure of a recent upper Bengal Fan-valley complex. In: Prather, B.E., Deptuck, M.E., Mohrig, D., van Hoorn, B., Wynn, R.B. (Eds.), Application of the Principles of Seismic Geomorphology to Continental Slope and Base of Slope Systems: Case Studies from Seafloor and Near-seafloor Analogues, vol. 99. SEPM Special Publication, pp. 347–369.

Leopold, L.B., Wolman, M.G., 1960. River meanders. GSA Bull. 71, 769–794.

Lien, T., Walker, R.G., Martinsen, O.J., 2003. Turbidites in the Upper Carboniferous Ross Formation, western Ireland: reconstruction of a channel and spillover system. Sedimentology 50, 113–148.

Macauley, R.V., Hubbard, S.M., 2013. Slope channel sedimentary processes and stratigraphic stacking, Cretaceous Tres Pasos Formation slope system, Chilean Patagonia. Mar. Petroleum Geol. 41, 146–162.

Maier, K.L., Fildani, A., Paull, C.K., Graham, S.A., McHargue, T.R., Caress, D.W., McGann, M., 2011. The elusive character of discontinuous deep-water channels: new insights from Lucia Chica channel system, offshore California. Geology 39, 327–330.

Maier, K.L., Fildani, A., McHargue, T.R., Paull, C.K., Graham, S.A., Caress, D.W., 2012. Punctuated deep-water channel migration: high-resolution subsurface data from the Lucia Chica channel system, offshore California, U.S.A. J. Sediment. Res. 82, 1–8.

Maier, K.L., Fildani, A., Paull, C.K., McHargue, T.R., Graham, S.A., Caress, D.W., 2013. Deep-water channel evolution and stratigraphic architecture from inception to abandonment from high-resolution Autonomous Underwater Vehicle surveys offshore central California. Sedimentology 60, 935–960.

Mayall, M., O'Byrne, C., 2002. Reservoir Prediction and Development Challenges in Turbidite Slope Channels. Offshore Technology Conference, Houston, OTC. Paper 14029.

Mayall, M., Jones, E., Casey, M., 2006. Turbidite channel reservoirs – key elements in facies prediction and effective development. Mar. Petroleum Geol. 23, 821–841.

McCulloch, D.S., 1987. Regional geology and hydrocarbon potential of offshore central California. In: Scholl, D.W., Grantz, A., Vedder, J.G. (Eds.), Geology and Resource Potential of the Continental Margin of Western North America and

Adjacent Ocean Basins—Beaufort Sea to Baja California, vol. 6. AAPG Circum-Pacific Council for Energy and Mineral Resources, pp. 353–401.

McHargue, T., Pyrcz, M.J., Sullivan, M.D., Clark, J., Fildani, A., Romans, B., Covault, J., Levy, M., Posamentier, H., Drinkwater, N., 2011. Architecture of turbidite channel systems on continental slope: patterns and predictions. Mar. Petroleum Geol. 28, 728–743.

McLelland, S.J., Ashworth, P.J., Best, J.L., Livesey, J.R., 1999. Turbulence and secondary flow over sediment stripes in weakly bimodal bed material. J. Hydraul. Eng. 125, 463–473.

Milne, J.A., 1983. Variation in cross-sectional asymmetry of coarse bedload river channels. Earth Surf. Process. Landf. 8, 503–511.

Moody, J.D., Pyles, D.R., Clark, J., Bouroullec, R., 2012. Quantitative outcrop characterization of an analog to weakly confined submarine channel systems: Morillo 1 member, Ainsa Basin, Spain. AAPG Bull. 96, 1813–1841.

Mutti, E., 1977. Distinctive thin-bedded turbidite facies and related depositional environments in the Eocene Hecho Group (South-Central Pyrenees, Spain). Sedimentology 24, 107–131.

Mutti, E., Normark, W.R., 1987. Comparing examples of modern and ancient turbidite systems: problems and concepts. In: Legget, J.K., Zuffa, G.G. (Eds.), Deep Water Clastic Deposits: Models and Case Histories. Marine Clastic Sedimentology, pp. 1–38.

Nakajima, T., Peakall, J., McCaffrey, W.D., Paton, D.A., Thompson, P.J., 2009. Outerbank bars: a new intra-channel architectural element within sinuous submarine slope channels. J. Sediment. Res. 79, 872–886.

Normark, W.R., 1970. Growth patterns of deep-sea fans. AAPG Bull. 54, 2170–2195.

O'Byrne, C.J., Barton, M.D., Steffens, G.S., Pirmez, C., Buergisser, H., 2007. Architecture of a laterally migrating channel complex: channel 4, Isaac Formation, Windermere Supergroup, Castle Creek North, British Columbia, Canada. In: Nilsen, T.H., Shew, R.D., Steffens, G.S., Studlick, J.R.J. (Eds.), Atlas of Deep-water Outcrops. AAPG Studies in Geology, vol 56, pp. 89–92.

Parsons, D.R., Peakall, J., Aksu, A.E., Flood, R.D., Hiscott, R.N., Beşiktepe, Ş., Mouland, D., 2010. Gravity-driven flows in a submarine channel bend: direct field evidence of helical flow reversal. Geology 38, 1063–1066.

Paull, C., Ussler, W., Maher, N., Greene, H.G., Rehder, G., Lorenson, T., Lee, H., 2002. Pockmarks off Big Sur, California. Mar. Geol. 181, 323–335.

Peakall, J., McCaffrey, B., Kneller, B., 2000. A process model for the evolution, morphology, and architecture of sinuous submarine channels. J. Sediment. Res. 70, 434–448.

Peakall, J., Amos, K.J., Keevil, G.M., Bradbury, P.W., Gupta, S., 2007. Flow processes and sedimentation in submarine channel bends. Mar. Petroleum Geol. 24, 470–486.

Peakall, J., Sumner, E.J., 2015. Submarine channel flow processes and deposits: a process-product perspective. Geomorphology 244, 95–120.

Pemberton, E.A.L., Hubbard, S.M., Fildani, A., Romans, B.W., Stright, L., 2016. The stratigraphic expression of decreasing confinement along a deep-water sediment routing system: outcrop example from southern Chile. Geosphere 12, 1–21.

Pickering, K.T., Coleman, J., Cremer, M., Droz, L., Kohl, B., Normark, W., O'Connell, S., Stow, D., Meyer-Wright, A., 1986. A high sinuosity, laterally migrating submarine fan channel–levee-overbank: results from DSDP Leg 96 on the Mississippi Fan, Gulf of Mexico. Mar. Petroleum Geol. 3, 3–18.

Pirmez, C., Flood, R.D., 1995. Morphology and structure of Amazon Channel. In: Flood, R.D., Piper, D.J.W., Klaus, A. (Eds.), Proceedings of the Ocean Drilling Program. Initial Reports 155. Ocean Drilling Program, College Station, Texas, pp. 23–45.

Pirmez, C., Beaubouef, R.T., Friedmann, S.J., Mohrig, D.C., 2000. Equilibrium profile and baselevel in submarine channels: examples from late Pleistocene systems and implications for the architecture of deepwater reservoirs. In: GCSSEPM Foundation 20th Annual Research Conference: Deep-water Reservoirs of the World.

Pirmez, C., Imran, J., 2003. Reconstruction of turbidity currents in Amazon Channel. Mar. Petroleum Geol. 20, 823–849.

Posamentier, H.W., Kolla, V., 2003. Seismic geomorphology and stratigraphy of depositional elements in deep-water settings. J. Sediment. Res. 73, 367–388.

Pringle, J.K., Brunt, R.L., Hodgson, D.M., Flint, S.S., 2010. Capturing stratigraphic and sedimentological complexity from submarine channel complex outcrops to digital 3D models, Karoo Basin, South Africa. Pet. Geosci. 16, 307–330.

Pyrcz, M.J., Sech, R.P., Covault, J.A., Willis, B.J., Sylvester, Z., Sun, T., 2015. Stratigraphic rule-based reservoir modeling. Can. Petroleum Geol. 63, 287–303.

Pyles, D.R., 2008. On the relationship between submarine channel sinuosity and symmetry, AAPG Annual Convention Abstract 90078. In: American Association of Petroleum Geologists Annual Convention, 20–23 April, San Antonio, Texas.

Pyles, D.R., Jennette, D.C., Tomasso, M., Beaubouef, R.T., Rossen, C., 2010. Concepts learned from a 3D outcrop of a sinuous slope channel complex: beacon channel complex, Brushy Canyon Formation, West Texas, U.S.A. J. Sediment. Res. 80, 67–96.

Romans, B.W., Hubbard, S.W., Graham, S.A., 2009. Stratigraphic evolution of an outcropping continental slope system, Tres Pasos Formation at Cerro Divisadero, Chile. Sedimentology 56, 737–764.

Romans, B.W., Fildani, A., Graham, S.A., Hubbard, S.M., Covault, J.A., 2010. Importance of predecessor basin history on the sedimentary fill of a retroarc foreland basin: provenance analysis of the Cretaceous Magallanes Basin, Chile (50-52°). Basin Res. 22, 640–658.

Samuel, A., Kneller, B., Raslan, S., Sharp, A., Parsons, C., 2003. Prolific deep-marine slope channels of the Nile Delta, Egypt. AAPG Bull. 87, 541–560.

Savoye, B., Cochonat, P., Apprioual, R., Bain, O., Baltzer, A., Bellec, V., Beuzart, P., Bourillet, J.-F., Cagna, R., Cremer, M., Crusson, A., Dennielou, B., Diebler, D., Droz, L., Ennes, J.-C., Floch, G., Guiomar, M., Harmegnies, F., Kerbrat, R., Klein, B., Kuhn, H., Landure, J.-Y., Lasnier, C., Le Drezen, E., Le Formal, J.-P., Lopez, M., Loubrieu, B., Marsset, T., Migeon, S., Normand, A., Nouze, H., Ondreas, H., Pelleau, P., Saget, P., Seranne, M., Sibuet, J.-C., Tofani, R., Voisset, M., 2000. Structure and recent evolution of the Zaire deepsea fan: preliminary results of the Zaiango 1 and 2 cruises (Angola- Congo margin). Earth Planet. Sci. 331, 211–220.

Schwartz, T.M., Graham, S.A., 2015. Stratigraphic architecture of a tide-influenced shelf-edge delta, Upper Cretaceous Dorotea Formation, Magallanes-Austral Basin, Patagonia. Sedimentology 64, 1039–1077.

Schwenk, T., Spieß, V., Hubscher, C., Breitzke, M., 2003. Frequent channel avulsions within the active channel–levee system of the middle Bengal Fan—an exceptional channel–levee development derived from Parasound and Hydrosweep data. Deep-Sea Res. II 50, 1023–1045.

Sheets, B.A., Paola, C., Kelberer, J.M., 2008. Creation and preservation of channel-form sand bodies in an experimental alluvial system. In: Nichols, G., Williams, E., Paola, C. (Eds.), Sedimentary Processes, Environments and Basins. A Tribute to Peter Friend, vol. 38. International Association of Sedimentologists Special Publication, pp. 555–567.

Shultz, M.R., Fildani, A., Cope, T.D., Graham, S.A., 2005. Deposition and stratigraphic architecture of an outcropping ancient slope system: Tres Pasos Formations, Magallanes Basin, southern Chile. In: Hodgson, D.M., Flint, S.S. (Eds.), Submarine Slope Systems: Processes and Products, vol. 244. Geological Society of London Special Publication, pp. 27–50.

Sprague, A.R., Sullivan, M.D., Campion, K.M., Jensen, G.N., Goulding, D.K., Sickafoose, D.K., Jennette, D.C., 2002. The physical stratigraphy of deep-water strata: a hierarchical approach to the analysis of genetically related elements for improved reservoir prediction. In: AAPG Annual Meeting Abstracts, Houston, Texas, pp. 10–13.

Straub, K.M., Mohrig, D., Buttles, J., McElroy, B., Pirmez, C., 2011. Quantifying the influence of channel sinuosity on the depositional mechanics of channelized turbidity currents: a laboratory study. Mar. Petroleum Geol. 28, 744–760.

Strong, N., Paola, C., 2008. Valleys that never were: time surfaces versus stratigraphic surfaces. J. Sediment. Res. 78, 579–593.

Sullivan, M., Jensen, G., Goulding, F., Jennette, D., Foreman, L., Stern, D., 2000. Architectural analysis of deep-water outcrops: implications for exploration and development of the Diana Subbasin, western Gulf of Mexico. In: Weimer, P., Slatt, R.M., Coleman, J., Rossen, C., Nelson, H., Bouma, A.H., Styzen, M.J., Lawrence, D.T. (Eds.), GCSSEPM Foundation 20th Annual Research Conference: Deep-water Reservoirs of the World, pp. 1010–1031.

Sumner, E.J., Peakall, J., Dorrell, R.M., Parsons, D.R., Wynn, R.B., Darby, S.E., McPhail, S.D., Perrett, J., Webb, A., White, D., 2014. Driven around the bend: spatial evolution and controls on the orientation of helical bend flow in a natural submarine gravity current. J. Geophys. Res. 119, 898–913.

Sylvester, Z., Pirmez, C., Cantelli, A., 2011. A model of submarine channel-levee evolution based on channel trajectories: implications for stratigraphic architecture. Mar. Petroleum Geol. 28, 716–727.

Sylvester, Z., Deptuck, M.E., Prather, B.E., Pirmez, C., O'Byrne, C., 2012. Seismic stratigraphy of a shelf-edge delta and linked submarine channels in the northeastern Gulf of Mexico. In: Prather, M.E., Deptuck, M.E., Mohrig, D., van Hoorn, B., Wynn, R. (Eds.), Application of the Principles of Seismic Geomorphology to Continental-Slope and Base-of-slope Systems: Case Studies from Seafloor and Near-seafloor Analogues, vol. 99. SEPM, Special Publication, pp. 31–59.

Thorne, C.E., Zevenbergen, L.W., Pitlick, J.C., Rais, S., Bradley, J.B., Julien, P.Y., 1985. Direct measurements of secondary currents in a meandering sand-bed river. Nature 315, 746–747.

Torres, J., Droz, L., Savoye, B., Terentieva, E., Cochonat, P., Kenyon, N.H., Canals, M., 1997. Deep-sea avulsion and morphosedimentary evolution of the Rhone Fan Valley and Neofan during the Late Quaternary (north-western Mediterranean Sea). Sedimentology 44, 457–477.

Wei, T., Peakall, J., Parsons, D.R., Chen, Z., Zhao, B., Best, J., 2013. Three-dimensional gravity current flow within a subaqueous bend: spatial evolution and force balance variations. Sedimentology 60, 241–247.

Wilson, T.J., 1991. Transition from back-arc to foreland basin development in southernmost Andes: stratigraphic record from the Ultima Esperanza District, Chile. GSA Bull. 103, 98–111.

Wynn, R.B., Cronin, B.T., Peakall, J., 2007. Sinuous deep-water channels: genesis, geometry and architecture. Mar. Petroleum Geol. 24, 341–387.